




# The high-energy transition state of the glutamate transporter homologue GltPh

Gerard H M Huysmans<sup>1,2,\*</sup> , Didar Ciftci<sup>1,3</sup>, Xiaoyu Wang<sup>1</sup>, Scott C Blanchard<sup>1,3,4</sup>  & Olga Boudker<sup>1,3,5,\*\*</sup> 

## Abstract

Membrane transporters mediate cellular uptake of nutrients, signaling molecules, and drugs. Their overall mechanisms are often well understood, but the structural features setting their rates are mostly unknown. Earlier single-molecule fluorescence imaging of the archaeal model glutamate transporter homologue Glt<sub>ph</sub> from *Pyrococcus horikoshii* suggested that the slow conformational transition from the outward- to the inward-facing state, when the bound substrate is translocated from the extracellular to the cytoplasmic side of the membrane, is rate limiting to transport. Here, we provide insight into the structure of the high-energy transition state of Glt<sub>ph</sub> that limits the rate of the substrate translocation process. Using bioinformatics, we identified Glt<sub>ph</sub> gain-of-function mutations in the flexible helical hairpin domain HP2 and applied linear free energy relationship analysis to infer that the transition state structurally resembles the inward-facing conformation. Based on these analyses, we propose an approach to search for allosteric modulators for transporters.

**Keywords** conformational dynamics; glutamate transporter; single-molecule fluorescence; static disorder; transition-state structure

**Subject Categories** Computational Biology; Membranes & Trafficking

**DOI** 10.15252/embj.2020105415 | Received 24 April 2020 | Revised 16 September 2020 | Accepted 18 September 2020 | Published online 13 November 2020

**The EMBO Journal (2021) 40: e105415**

## Introduction

The fluxes of small molecules across biological membranes mediated by membrane-embedded transporters are essential to life, and their dysregulation leads to numerous diseases (Cesar-Razquin, Snijder *et al.*, 2015). High-resolution structures of transporters have revealed conformations that expose substrate-binding sites to the opposite sides of the membrane, providing a structural rationale for the alternating access mechanism (Drew & Boudker, 2016). In contrast, we

know relatively little about the structures of high-energy transition states (TSs) that are essential to understand the kinetic mechanisms, how the kinetics are affected by post-translational modifications, or small-molecule modulators (Kortagere, Fontana *et al.*, 2013; Li, Hasenhuettl *et al.*, 2015; Czuba, Hillgren *et al.*, 2018) or how to develop drugs that modulate transporter activities (Rives, Javitch *et al.*, 2017). While many computational approaches are used to map the energy landscapes of the transporters (Weng, Fan *et al.*, 2010; Espinoza-Fonseca & Thomas, 2011; Jiang, Shrivastava *et al.*, 2011; Stolzenberg, Khelashvili *et al.*, 2012; Weng, Fan *et al.*, 2012; Gur, Zomot *et al.*, 2013; Stelzl, Fowler *et al.*, 2014; Gur, Zomot *et al.*, 2015; Moradi, Enkavi *et al.*, 2015; Liao, Marinelli *et al.*, 2016; Cheng, Kaya *et al.*, 2018; Selvam, Mittal *et al.*, 2018; Wang, Albers *et al.*, 2018), experimental data reporting on TSs are scarce (Leninger, Sae Her *et al.*, 2019; Wu, Wynne *et al.*, 2019).

TSs are only transiently populated and cannot be studied by direct structural methods. However, linear free energy relationship (LFER) analyses provided insights into the TSs of enzyme reactions (Fersht & Wells, 1991; Hollfelder & Herschlag, 1995; Mihai, Kravchuk *et al.*, 2003), protein folding (Matouschek, Kellis *et al.*, 1989; Curnow & Booth, 2009; Huysmans, Baldwin *et al.*, 2010; Schleich, Woodall *et al.*, 2014; Paslawski, Lillelund *et al.*, 2015), and channel opening (Grosman, Zhou *et al.*, 2000; Auerbach, 2003; Sorum, Czege *et al.*, 2015). LFERs correlate the effects of amino acid substitutions and ligands on the reaction rates to the changes in the equilibrium constant for an observed transition. From these correlations, one can infer whether the perturbed region of the protein resembles the initial or the final conformation in the TS (Evans & Polanyi, 1936; Leffler, 1953; Fersht & Sato, 2004). Here, we use LFERs to characterize the structure of the TS during substrate translocation by Glt<sub>ph</sub>, an aspartate/sodium symporter from the hyperthermophilic archaeobacterium *Pyrococcus horikoshii*.

Glt<sub>ph</sub> is an extensively studied homologue of human excitatory amino acid transporters (EAATs) (Vandenberg & Ryan, 2013). It utilizes the physiological transmembrane sodium (Na<sup>+</sup>) gradient by symporting one aspartate (*L*-Asp) and three Na<sup>+</sup> ions (Boudker, Ryan *et al.*, 2007; Ryan, Compton *et al.*, 2009; Groeneveld &

1 Department of Physiology and Biophysics, Weill Cornell Medicine, New York, NY, USA

2 Mass Spectrometry for Biology Unit, USR 2000, CNRS, Institut Pasteur, Paris, France

3 Tri-Institutional Training Program in Chemical Biology, New York, NY, USA

4 St. Jude Children's Research Hospital, Memphis, TN, USA

5 Howard Hughes Medical Institute, Chevy Chase, MD, USA

\*Corresponding author. Tel: +1 212 746 6941; E-mail: ghh2001@med.cornell.edu

\*\*Corresponding author. Tel: +1 212 746 6634; E-mail: olb2003@med.cornell.edu

Slotboom, 2010). The mechanism of  $\text{Glt}_{\text{Ph}}$  is well understood from a structural perspective.  $\text{Glt}_{\text{Ph}}$  is a homotrimer, with each protomer consisting of a trimerization scaffold domain and a transport domain, containing the L-Asp- and  $\text{Na}^+$ -binding sites. A  $\sim 15 \text{ \AA}$  “elevator” movement of the transport domain along the membrane normal from an outward-facing state (OFS) to an inward-facing state (IFS) delivers solutes across the bilayer (Fig 1A) (Yernool, Boudker

et al, 2004; Akyuz, Altman et al, 2013; Erkens, Hanelt et al, 2013; Georgieva, Borbat et al, 2013; Hanelt, Wunnicke et al, 2013; Akyuz, Georgieva et al, 2015; Hanelt, Jensen et al, 2015; Guskov, Jensen et al, 2016; Canul-Tec, Assal et al, 2017; Ruan, Miyagi et al, 2017; Arkhipova, Trinco et al, 2019). During this transition, the transport domain forms two alternative interfaces with the scaffold involving pseudosymmetric helical hairpins 1 and 2 (HP1 and HP2) (Yernool

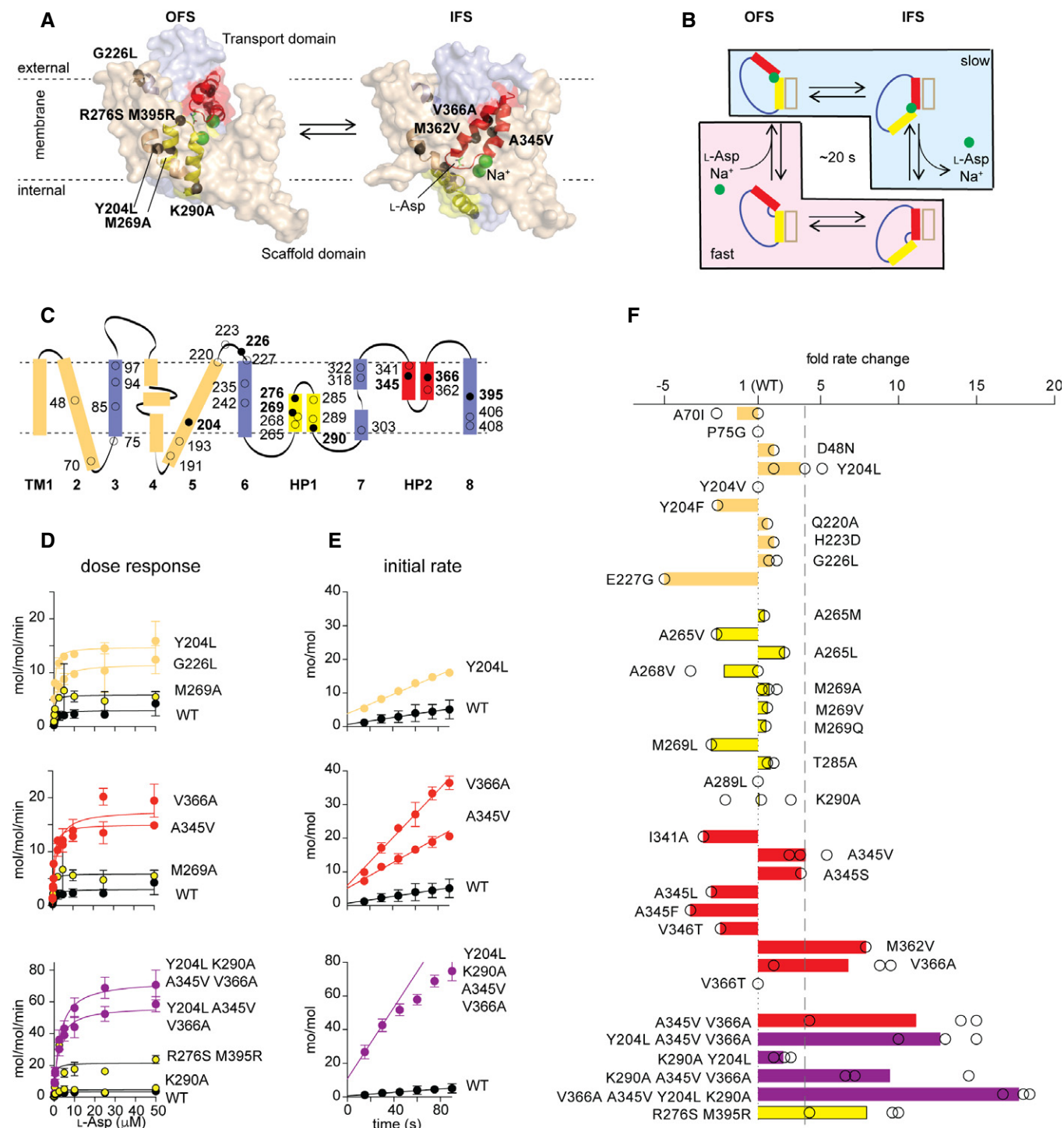


Figure 1.

**Figure 1. Gain-of-function Glt<sub>ph</sub> variants.**

- A A Glt<sub>ph</sub> protomer in the OFS and IFS is shown in semitransparent surface representation with the scaffold and transport domains colored wheat and blue, respectively. HP1 (yellow) and HP2 (red) are emphasized as cartoons. Bound L-Asp and Na<sup>+</sup> ions are shown as green sticks and spheres, respectively. Select amino acids mutated in this study are shown as black spheres.
- B Schematic representation of the Glt<sub>ph</sub> transport cycle showing one protomer. Comparatively rapid and slow steps of the cycle are shaded pink and blue, respectively.
- C The topology of a Glt<sub>ph</sub> protomer showing tested mutation sites (circles) with filled circles corresponding to those shown in (A).
- D, E Representative examples of dose–response curves and time courses. Lines through the dose–response curves are fits to the Michaelis–Menten equation; time courses are fitted to linear equations. Shown are means and standard errors over at least three independent repeats.
- F Fold increase (positive values) or decrease (negative values) in the initial uptake rates of the variants relative to WT Glt<sub>ph</sub>. Circles are averages of technical triplicates. Bars are means over independent repeats (as indicated). The dashed line marks a fourfold increase in the initial rate.

Data information: Color coding is the same in all panels. In (D–F), data are colored according to the structural elements where the mutations are located; combination mutants are colored purple. See also Appendix Fig S1 and Appendix Tables S1 and S2.

*et al*, 2004; Crisman, Qu *et al*, 2009; Reyes, Ginter *et al*, 2009). HP1 is sandwiched between the transport and scaffold domains, and HP2 lines the extracellular surface of the protomer in the OFS. In contrast, HP2 is positioned on the interface, and HP1 faces the cytosol in the IFS (Fig 1A). HP2 forms a lid over the substrate-binding site and serves as the extracellular gate (Boudker *et al*, 2007; Huang & Tajkhorshid, 2008; Shrivastava, Jiang *et al*, 2008; Grazioso, Limongelli *et al*, 2012; Heinzlmann, Bastug *et al*, 2013; Zomot & Bahar, 2013; Verdon, Oh *et al*, 2014). Following the release of L-Asp and Na<sup>+</sup> ions in the IFS via an incompletely understood mechanism, HP2 collapses onto the substrate-binding site (Oh & Boudker, 2018; Garaeva, Guskov *et al*, 2019). The return of the transport domain to the OFS completes the cycle (Fig 1B). Time-resolved single-molecule Förster resonance energy transfer (smFRET) recordings established the key features of the elevator movements of the transport domains (Akyuz *et al*, 2013; Erkens *et al*, 2013; Akyuz *et al*, 2015). These studies suggested that the translocation of the substrate-loaded transport domain from the OFS to the IFS is the rate limiting step of the cycle, but the nature of the high-energy rate-determining barrier remained unknown.

Here, we generated a repertoire of gain-of-function Glt<sub>ph</sub> mutants, in part, through the analysis of systematic amino acid sequence variations among glutamate transporters from organisms living at different temperatures. Our fastest mutant showed the substrate uptake rate ~20-fold higher than the wild-type (WT) transporter. Close examination of a representative set of these mutants corroborated previous findings that an increased rate of elevator transitions of the substrate-loaded transport domain was necessary to increase uptake rate (Akyuz *et al*, 2015), but also showed that the more dynamic mutants benefited from reduced substrate affinity. At the single-molecule level, the transport domain dynamics of WT and mutant Glt<sub>ph</sub> were highly heterogeneous, showing a broad distribution of transition frequencies between individual molecules in the population. These apparent dynamic modes parallel the activity modes observed in a recently developed single-molecule transport assay (Ciftci *et al*, 2020).

We focused on the dynamic mode in which all examined Glt<sub>ph</sub> variants spend most of their time to probe the most commonly crossed TS structure. All mutations that increased elevator dynamics increased the rate of the OFS-to-IFS transitions, but most did not affect the rate of the reverse reaction. Based on these observations, the LFER analysis predicts that the high-energy TS structurally resembles the IFS. Thus, our data suggest that the transport domain might make multiple attempts at reaching the IFS-like TS during the OFS residence before progressing to the stable observable IFS. We

propose that small molecules with a higher affinity for the IFS than the OFS would also have a higher affinity for the TS. These molecules would, therefore, lower the height of the energy barrier of the OFS to the IFS transition and speed up transport. Our study provides a “recipe” for the possible development of positive allosteric modulators of human transporters.

## Results

### Gain-of-function mutations

Originating from a hyperthermophile, Glt<sub>ph</sub> is a slow transporter (Boudker *et al*, 2007; Ryan *et al*, 2009) (Fig 1B). This property is in line with observations that enzymes from thermophilic organisms, which evolved to be stable and functional at high temperatures, show low activity at ambient temperature (Somero, 2004; Elias, Wiczorek *et al*, 2014). Consistently, glutamate transporters from mesophilic bacteria are more active than Glt<sub>ph</sub> (Tolner, Ubbink-Kok *et al*, 1995; Gaillard, Slotboom *et al*, 1996; Yernool, Boudker *et al*, 2003; Rahman, Ismat *et al*, 2017). Also, structurally very similar human EAATs (Canul-Tec *et al*, 2017) are ~20 to 10,000-fold faster (Vandenberg & Ryan, 2013). Interestingly, a “humanizing” R276S/M395R mutation in Glt<sub>ph</sub>, which moves an arginine proximal to the substrate-binding site from its location in Glt<sub>ph</sub> to that in EAATs, confers an increased transport rate (Ryan, Kortt *et al*, 2010). Inspired by these considerations, we searched for additional gain-of-function mutations by identifying potential evolutionary adaptations to achieve higher activity at lower temperatures. We constructed a multiple sequence alignment of prokaryotic glutamate transporters sorted by the optimum growth temperature of their species of origin and looked for systematic variations between sequences from hyperthermophiles, thermophiles, mesophiles, and psychrophiles (Appendix Fig S1). Overall, we did not observe highly significant systematic changes across all sequences, suggesting that different mutations occurred in different evolutionary lineages. Nevertheless, when we mapped residues with positive global differences scores (Methods and Appendix Table S1) onto the structure of Glt<sub>ph</sub>, we found that the majority formed two clusters in the transport domain centered on HP1 and HP2 (Appendix Fig S1 and Appendix Table S1). Among these, sites with a preference for smaller amino acids in hyperthermophiles were more likely to be taken by larger amino acids in mesophiles and psychrophiles and *vice versa* (Appendix Table S1). Thus, the packing interactions within the transport domain might play a role during temperature adaptation, consistent

with earlier studies where thermophilic and psychrophilic enzymes were, respectively, more rigid and more dynamic than their mesophilic counterparts (Low, Bada *et al*, 1973; Feller, 2010).

Using this analysis, but also expanding into other regions of the protein (Appendix Fig S1), we selected 30 sites (Fig 1C) and tested the transport activity of 44 single mutants reconstituted into proteoliposomes (Appendix Table S2). A majority showed  $K_M$  values for L-Asp similar to the WT  $K_M$  of  $0.5 \pm 0.04 \mu\text{M}$ , but different maximal rates (Fig 1D, Appendix Table S2). We subsequently measured the initial transport rates of all mutants at L-Asp concentrations of fivefold over the  $K_M$  values (Fig 1E and F). Five mutations increased the transport rate at least fourfold (Fig 1F, Appendix Table S2). Four of these (A345V, A345S, M362V, and V366A) were in HP2 with A345 and V366 sites identified by the bioinformatics analysis (Appendix Fig S1, Appendix Table S1). All four increased  $K_M$  at least twofold. The fifth mutation, Y204L Glt<sub>ph</sub>, is located to the kink of TM5 in the scaffold domain (Fig 1A and F, Appendix Table S2). This site did not receive a high score in our analysis because ~80% of the bacterial sequences already have an aliphatic residue at this position, but is notable because the flexibility of the kink might facilitate elevator movements (Verdon & Boudker, 2012). Mutations elsewhere failed to boost transport (Fig 1F, Appendix Table S2). Among these were mutations in and around HP1, suggesting that HP1 and HP2 do not share similar functional roles despite structural pseudosymmetry. Mutations designed to increase interdomain hinge flexibility (P75G and E227G) also did little to boost activity, suggesting that hinges are already sufficiently dynamic even in thermophilic glutamate transporters. Combining the three gain-of-function mutations, Y204L, A345V, and V366A produced a mutant with activity  $12.7 \pm 2.5$  times higher than WT Glt<sub>ph</sub> (Fig 1E and F and Appendix Table S2). Thus, subtle packing mutations in HP2 and the scaffold TM5 increase the transport rate by an order of magnitude.

No other combinations produced further rate improvements, including those with the “humanizing” R276S/M395R mutations (Appendix Table S2). To further boost transport, we considered the K290A mutation on HP1 (Fig 1A and E), which disrupts a salt bridge with E192 on the scaffold in the OFS and increases the transport domain dynamics (Akyuz *et al*, 2013; Georgieva *et al*, 2013). The K290A mutation by itself did not affect the transport rate. However, when combined with the Y204L/A345V/V366A mutant, it yielded our most active variant with an  $18 \pm 1$  times faster uptake rate than WT Glt<sub>ph</sub> and mean turnover time of ~1 s (Fig 1E and F, and Appendix Table S2).

These robust, 10–20-fold, increases in transport rate in a set of Glt<sub>ph</sub> variants that contain at most four mutations are in line with similar efforts in enzymology (Renosto, Schultz *et al*, 1985; Thomas & Scopes, 1998; Johns & Somero, 2004; Dick, Weiergraber *et al*, 2016; Nguyen, Wilson *et al*, 2017; Saavedra, Wrabl *et al*, 2018; Akanuma, Bessho *et al*, 2019).

### Rate limiting steps of the transport cycle

To identify rate limiting features of the transport mechanism, we followed the timing of the transport domain movements between the OFS and IFS by smFRET, using total internal reflection fluorescence (TIRF) microscopy (Akyuz *et al*, 2013; Erkens *et al*, 2013; Akyuz *et al*, 2015; Juetter, Terry *et al*, 2016). We labeled a single cysteine mutant (N378C) within the transport domain with self-healing

fluorophores LD555P-MAL and LD655-MAL, and biotin–polyethylene glycol–maleimide. We then reconstituted the transporters into proteoliposomes and immobilized them via a streptavidin–biotin bridge in microfluidic perfusion chambers enabling rapid buffer exchange (Appendix Fig S2). We monitored the relative movements of the donor- and acceptor-labeled transport domains within the trimeric transporters at 100-ms time resolution for a mean duration of ~70 s before photobleaching occurred. Measured FRET efficiency ( $E_{\text{FRET}}$ ) of ~0.4 corresponded to both transport domains in the OFS.  $E_{\text{FRET}}$  increased to ~0.6 and ~0.9 when, respectively, one or both isomerized into the IFS (Appendix Fig S2). Typically, only one protomer at a time displays recurring transitions between  $E_{\text{FRET}}$  of ~0.4 and ~0.6 or less often between ~0.6 and ~0.9 during the observation time (Akyuz *et al*, 2013; Akyuz *et al*, 2015).

The transport domains shuttled between the OFS and IFS with a mean frequency of  $0.35 \pm 0.01 \text{ s}^{-1}$  in apo WT Glt<sub>ph</sub> in proteoliposomes in which external and internal buffers contained no Na<sup>+</sup> ions or L-Asp (Fig 2A). The transport domain dynamics were dramatically reduced to a mean frequency of  $0.04 \pm 0.01 \text{ s}^{-1}$  when we replaced the external buffer with a buffer containing saturating concentrations of Na<sup>+</sup> ions and L-Asp to establish the chemical gradients required for transport (Fig 2B). The dynamics of the Glt<sub>ph</sub> mutants showed similar overall features and trends. All variants exhibited comparatively fast dynamics under apo conditions with frequencies between ~0.24 and  $0.6 \text{ s}^{-1}$  (Fig 2A and Appendix Fig S3), which decreased to different extents under transport conditions, except in R276S/M395R Glt<sub>ph</sub> (Figs 2B and Appendix Fig S4). In the presence of 10 mM blocker, D, L-threo-β-benzyloxyaspartic acid (D,L-TBOA), which should suppress all transitions, we still observed a transition frequency of  $0.03 \pm 0.01 \text{ s}^{-1}$  in both WT and mutant Glt<sub>ph</sub> proteins (Appendix Table S3). However, these transitions originated from only ~8–17% of all molecules, leading us to suspect that these transitions reflect functionally defective transporters unable to bind D,L-TBOA, or from spurious blocker dissociation (Akyuz *et al*, 2013; Akyuz *et al*, 2015). When we subtracted this small sub-population from the measured transition frequencies, the resulting frequency for the WT Glt<sub>ph</sub> at room temperature reduced to ~0.01 s<sup>-1</sup>, on par with the transport turnover rate of  $0.06 \text{ s}^{-1}$  measured at 34°C (Appendix Table S2) and the mean single-transporter rate of  $0.01 \text{ s}^{-1}$  measured at 20°C (Ciftci *et al*, 2020). Overall, these results are consistent with the earlier measurements showing that the substrate-loaded transport domain is significantly less dynamic than the apo domain and that its movements occur with rates similar to the uptake rates (Akyuz *et al*, 2013; Akyuz *et al*, 2015).

We observed correlated increases in dynamics and L-Asp uptake rates in several mutants (Fig 3A). For instance, Y204L/A345V/V366A Glt<sub>ph</sub> showed the mean transition frequency, and the uptake rate increased by 12- and 13-fold, respectively. In contrast, the K290A and K290A/Y204L Glt<sub>ph</sub> mutants showed a ~30-fold increase in dynamics but no significant changes in activity (Fig 3A). We speculate that substrate release from the IFS becomes rate limiting in these dynamic mutants, with the transport domain visiting IFS multiple times before releasing substrate (Fig 1B).

The following considerations substantiate the hypothesis. Y204L and K290A did not affect the L-Asp affinity, consistent with unaltered  $K_M$  values (Fig 3A and Appendix Fig S5). In contrast, A345V, V366A, and the R276S/M395R mutations reduced affinity ~10, 150, and 40 times, respectively. Most remarkably, combining mutations

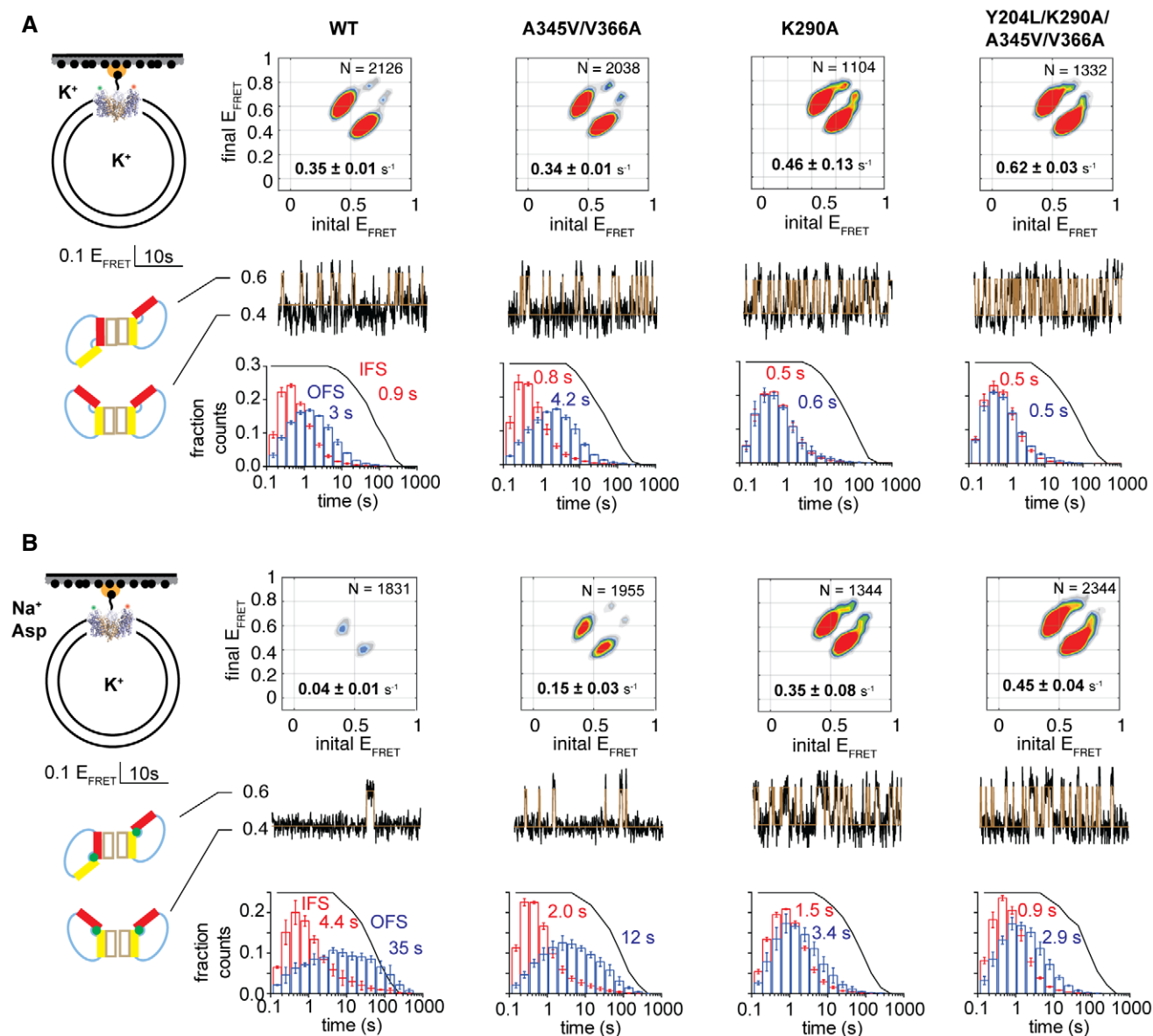


**Figure 2. Transport domain dynamics under apo (A) and transport (B) conditions.**

A, B Schematic representations of the experimental conditions are shown on the far left. Data are shown for WT Glt<sub>ph</sub> and select gain-of-function mutants, as indicated above the panels. Transition density plots (top of each panel) show the frequency of transitions between the  $E_{FRET}$  values. The number of trajectories analyzed ( $N$ ) and the population-wide mean frequency of transitions are shown on the panels. Representative 50-s sections of single-molecule  $E_{FRET}$  trajectories (middle) with raw data in black and idealizations in brown. Scale bar and the conformational states corresponding to the low and intermediate  $E_{FRET}$  values are shown to the left of the panels. Dwell-time distributions for the OFS in blue and the IFS in red (bottom). Mean dwell times are shown on the panels in corresponding colors. Black lines represent photobleaching survival plots normalized from 1 to 0. Shown are means and standard errors over at least three independent repeats. See also Appendix Figs S2–S4.

that dramatically increased the transition frequency (K290A and K290A/Y204L) with those that reduced L-Asp affinity (A345V and V366A) yielded the fastest Glt<sub>ph</sub> variants (Fig 3A). Therefore, we speculate that A345V, V366A, and R276S/M395R mutations increase the L-Asp dissociation rates, decreasing the affinity and allowing the mutants to achieve rates limited by the elevator dynamics.

It is, in principle, possible that Na<sup>+</sup> and L-Asp binding to the OFS is rate limiting in the dynamic mutants. However, it is unlikely because Na<sup>+</sup> binding to the OFS, rate limiting for L-Asp binding,

occurs within a second under our experimental conditions (Hanelt *et al*, 2015). Furthermore, we observed dramatically longer OFS dwell times under transport conditions compared to apo conditions (Fig 2). If Na<sup>+</sup> binding to the OFS were slow, we would have expected to observe many more apo-like short OFS dwells, as the domains moved inward before binding solutes. Notably, in our fastest Y204L/K290A/A345V/V366A mutant, achieving turnovers of 1 s, all rate constants become similar, and substrate binding might also impact the transport rate.

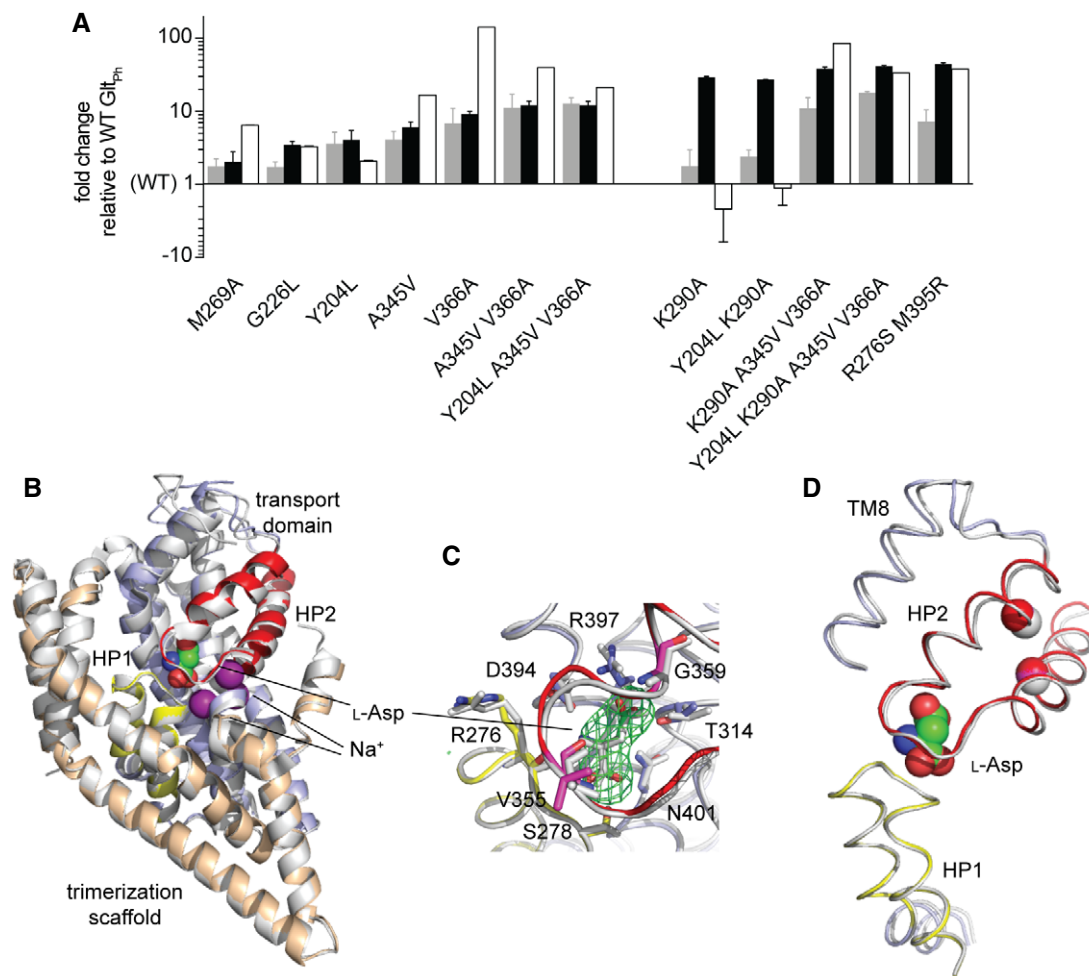


**Figure 3. Correlations between activity, dynamics, and substrate affinity.**

- A** Changes in the initial rates of substrate uptake (gray bars), transport domain dynamics (black bars), and L-Asp dissociation constant (white bars) of the mutant Glt<sub>ph</sub> variants relative to the WT transporter. The transition frequencies were measured under non-equilibrium transport conditions, and frequencies obtained in the presence of D,L-TBOA were subtracted from the data. Error bars represent standard errors for at least three independent measurements.
- B** Cartoon representation of the crystal structure of Y204L/A345V/V366A Glt<sub>ph</sub> in the presence of saturating concentrations of Na<sup>+</sup> ions and L-Asp (colored as in Fig 1A; PDB accession number: 6V8G) superimposed onto the structure of WT Glt<sub>ph</sub> in the OFS (gray, PDB accession number: 2NWX). L-Asp and Na<sup>+</sup> are shown as spheres and colored by atom type.
- C** Close-up of the substrate-binding site. Green mesh represents an omit electron density map for L-Asp contoured at 4 $\sigma$ . Substrate-coordinating residues are shown as sticks.
- D** Superimposition of the mutant (colors) and the WT (gray) hairpins aligned on HP1. See also Appendix Figs S4 and S5 and Appendix Tables S2–S4.

HP2 packing mutations A345V and V366A are striking because they both increase the transport domain dynamics and reduce L-Asp affinity. The altered affinity was unexpected because the residues are located ~14 Å away from the binding site (Appendix Fig S1). The crystal structure of the Y204L/A345V/V366A mutant at ~3.4 Å resolution showed the transporter in an OFS conformation nearly identical to that of the WT (Fig 3B and D, Appendix Table S4). The electron density for L-Asp was visible, and the amino acid coordination was unaltered (Fig 3C). Interestingly, the unusually high B-factors of residues in HP2 and the adjacent part of TM8 suggested positional disorder in this region (Appendix Fig S5). One notable difference from the WT structure was the position of the loop connecting TMs 3 and 4. The

electron density was unresolved for the bulk of the loop, but a stretch of nine modeled N-terminal residues ran toward the top of the transport domain, instead of crossing over the HP2 surface as in WT Glt<sub>ph</sub> (Appendix Fig S5). A similar loop conformation was seen in the crystal structure where the transport domain adopted an intermediate position between the OFS and the IFS (Verdon & Boudker, 2012). It remains unclear whether the observed loop conformations are consequences of different crystal packing or have functional implications (Compton, Taylor *et al*, 2010; Mulligan & Mindell, 2013). Overall, the mutations do not change the structure of HP2 or the binding site but might affect the local dynamics. If so, the reduced affinity could be due to the increased entropic penalty incurred upon substrate binding to a more

dynamic apo protein or a less effective water exclusion from the binding site.

### The predominant mode of the transport domain dynamics

We used smFRET recordings at saturating Na<sup>+</sup> and L-Asp concentrations on both sides of the liposomal membrane (Appendix Fig S6) to study the energy barrier controlling the rate of substrate translocation. As observed in earlier studies (Akyuz *et al*, 2015), WT GlT<sub>ph</sub> dynamics were highly heterogeneous, with the OFS and IFS dwell times ranging from shorter than a second to hundreds of seconds

(Fig 4A). At least three exponentials were required to fit the cumulative survival plots (Appendix Fig S6), yielding lifetimes for the OFS of ~3, 20, and 85 s, with each component contributing equally to the fit (Appendix Fig S6). The IFS survival plots showed similar features, except that the short lifetime component was more prevalent (Appendix Fig S6). The longest OFS dwells were shorter in more dynamic mutants, and this change was most dramatic in variants carrying the K290A and R276S/M395R mutations (Fig 4A and Appendix Fig S6). Recordings performed with 10-ms time resolution showed similar state distributions. They also revealed only a few dwells shorter than 300 ms in the OFS and more in the IFS.

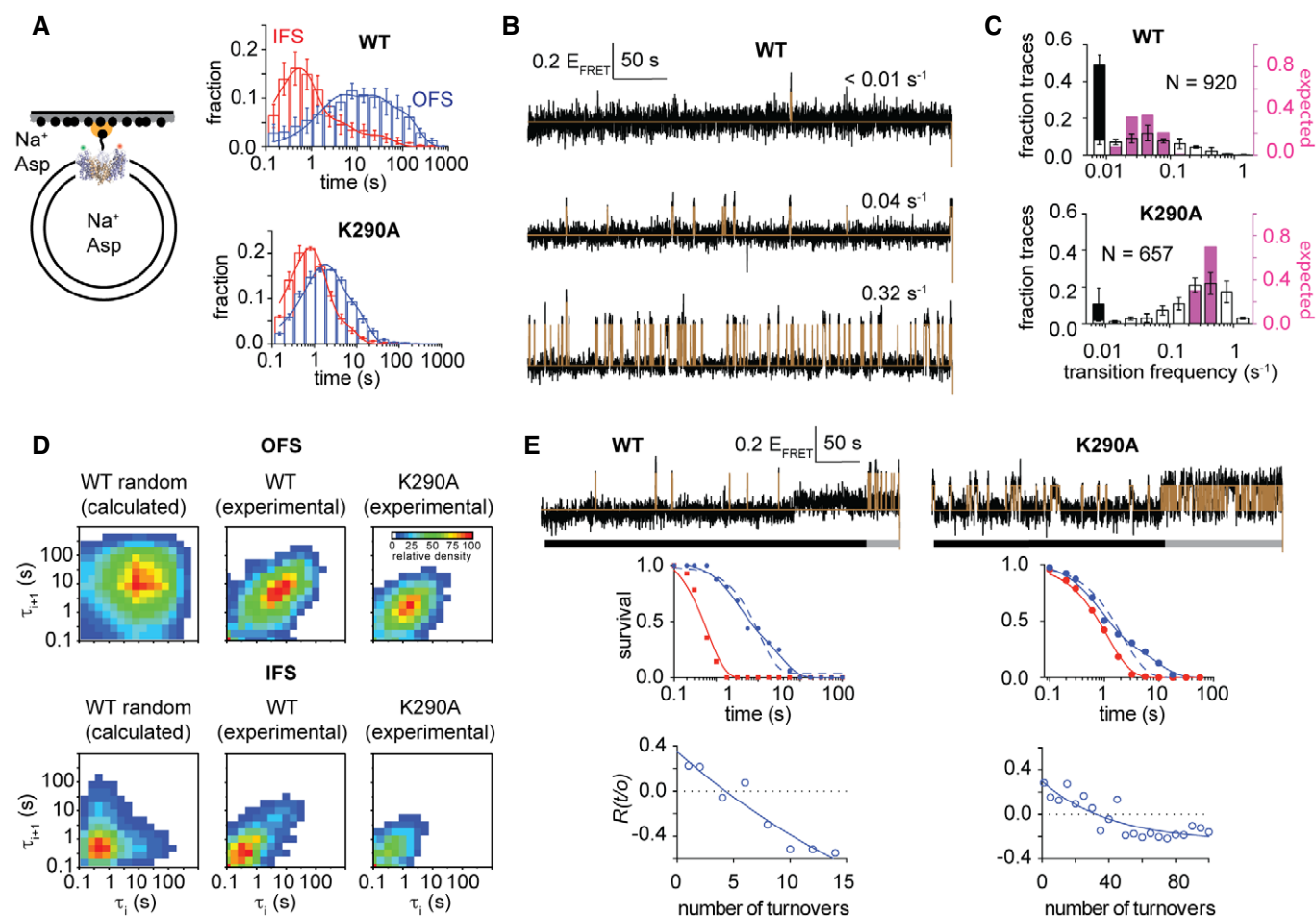


**Figure 4. Kinetic heterogeneity of the transport domain dynamics.**

A Dwell-time distributions of the OFS (blue) and the IFS (red) for WT (top) and K290A (bottom) GlT<sub>ph</sub> observed under equilibrium conditions in saturating Na<sup>+</sup>/L-Asp (left). Lines are fits to three exponentials. Data are averages and standard errors of at least three independent measurements.

B Representative  $E_{\text{FRET}}$  trajectories of WT GlT<sub>ph</sub> showing different transition frequencies. Raw data are in black, and idealizations are in brown. Scale bar is above the trajectories.

C Distribution of the WT (top) and the K290A GlT<sub>ph</sub> (bottom) molecules with different mean transition frequencies (white bars).  $N$  is the number of trajectories longer than 90 s used in the analysis. The stacked black bars are fractions of trajectories without transitions. Pink bars show the expected binomial distribution if all trajectories shared the mean transition frequency of 0.04 s<sup>-1</sup> for the WT and 0.34 s<sup>-1</sup> for the K290A. Data are averages and standard errors of at least three independent measurements.

D 2D histograms of the consecutive dwell lengths in the OFS (top) and the IFS (bottom). From left to right: calculated distribution of dwell times randomly selected from the distributions in panel A; measured distribution for WT GlT<sub>ph</sub> and the K290A mutant.

E Representative trajectories of the WT (left) and the K290A (right) GlT<sub>ph</sub> molecules showing switching between dynamic modes. Raw data are in black, and idealizations are in brown (top). Black and gray bars under the trajectories indicate apparent slower and faster dynamic modes. Survival plots for the OFS and the IFS (middle). Solid lines are fits to a single (IFS) and double (OFS) exponentials. Dashed lines (OFS only) are rejected fits to single exponentials. Autocorrelation plots of the sequential dwell durations (bottom). Solid lines are fits to single exponentials to guide the eye. See also Appendix Figs S6–S9.

Therefore, 100-ms time resolution is sufficient to capture most, but not all, elevator transitions (Appendix Fig S7). To account for missed transitions, we mathematically corrected the estimated FRET-state lifetimes following established procedures (Blatz & Magleby, 1986). Consistent with a 100-ms frame rate being appropriate for the present analyses, missed-event considerations had little impact on the actual FRET-state lifetimes.

Strikingly, some smFRET traces for the WT transporter showed no or rare transitions, while others featured sustained dynamics (Fig 4B). When we calculated transition frequencies for the individual traces lasting longer than 90 s before photobleaching, we obtained a distribution spanning over two orders of magnitude (Fig 4C). This distribution is significantly broader than would be expected if dwells occurred randomly, with all molecules having the same intrinsic dynamics (Fig 4C). Broader than expected transition frequency distributions were observed for all examined mutants (Fig 4C and Appendix Fig S8). These data indicate that the dynamics of all Glt<sub>ph</sub> variants are characterized by static disorder (Zwanzig, 1990), i.e., distinct kinetic behaviors persist for periods of time comparable to or longer than the observation window. Consistently, we observed correlated lengths of the consecutive dwells in all variants (Fig 4D and Appendix Fig S9).

Importantly, the majority of the individual traces showed intrinsically homogeneous dynamics. Their OFS and IFS survival plots were fitted well by single exponentials (Appendix Fig S10), and their dwell lengths varied randomly around the means as revealed by the flat autocorrelation functions (Lu, Xun *et al*, 1998) (Appendix Fig S10). Only in a minor fraction of molecules, ranging between 5 and 20 %, survival plots fitted better to two exponentials. Notably, in a subset of these molecules, we observed an apparent switching from one dynamic mode to another, which resulted in autocorrelation functions indicative of temporal segregation of similar dwells (Fig 4E and Appendix Fig S10). These results are generally in agreement with our earlier recordings that showed that the transporters sampled dynamic states and also long-lasting quiescent states (Akyuz *et al*, 2015), which we attributed to distinct off-pathway “locked” conformations. In our current recordings, which are approximately three times longer due to the improved stability of the self-healing fluorophores (Altman, Zheng *et al*, 2012; Zheng, Jockusch *et al*, 2014), we observe that the previously described “locked” states can transition into the IFS, but with low frequency.

Following this analysis, each Glt<sub>ph</sub> transporter with intrinsically homogeneous dynamics can be described by a pair of characteristic OFS and IFS lifetimes mathematically corrected for the missed transitions (Blatz & Magleby, 1986). When plotted on a 2D histogram, they visualize the kinetic heterogeneity of the entire population (Fig 5A and Appendix Fig S11). For WT Glt<sub>ph</sub>, the histogram showed that “typical” molecules had long OFS lifetimes, ranging from ~ 10 to 100 s, and short IFS lifetimes between ~0.5 and 2 s (Fig 5A and Appendix Fig S11). The same kinetic mode prevailed in all of the mutants (Fig 5B and C). Some mutants, most strikingly A345V and V366A Glt<sub>ph</sub>, also had an increased fraction of transporters with long IFS and very short OFS lifetimes (Fig 5B and Appendix Fig S11). At present, the functional significance of these distinct kinetic behaviors is unclear. Consistent with this observation, recently established single-molecule transport assays have also revealed that WT Glt<sub>ph</sub> exhibits a broad kinetic heterogeneity, with individual transporters showing turnover times between seconds

and hundreds of seconds (Ciftci *et al*, 2020). Thus, the multiple kinetic modes of the conformational dynamics appear to parallel the multiple transport activity modes.

The observed kinetic heterogeneity is unlikely to be due to post-translational modifications or differences in the lipid environments between individual vesicles because it is reduced under apo conditions (Appendix Fig S12 and Appendix Fig S13). It is also unlikely to arise from incompletely saturated Na<sup>+</sup> sites because we used ion concentrations in excess of 200-fold over the  $K_D$  values (Reyes, Oh *et al*, 2013). Instead, we hypothesize that the heterogeneity is indicative of a highly rugged energy landscape and the existence of long-lived conformations with distinct kinetic properties. Kinetic heterogeneities have been reported in many cases (Auerbach & Lingle, 1986; Xue & Yeung, 1995; Lu *et al*, 1998; Zhuang, Kim *et al*, 2002; Nayak, Dana *et al*, 2011; Min, Jefferson *et al*, 2018; Zosel, Mercadante *et al*, 2018). However, they might be particularly pronounced in Glt<sub>ph</sub> because it is a thermophilic protein that might encounter high enthalpic barriers at ambient temperatures. To gain insight into the nature of the most commonly used activation barrier during elevator motions, we set out to perform TS analyses on the predominant observed dynamic mode. Other dynamic modes, such as the one with short OFS and long IFS lifetimes (Fig 5A and B), might have distinct TSs.

### Transition-state structure

While the macroscopic rates of the transport domain translocation are slow, the translocation process itself is faster than the resolution of our smFRET recordings (10–100 ms). Correspondingly, intermediate positions of the domain, manifesting in intermediate  $E_{FRET}$  values, are not observed even though they must be traversed on a faster timescale (Chung, McHale *et al*, 2012; Chung, Piana-Agostinetti *et al*, 2015). The long dwell times in the OFS and IFS arise from the high-energy barrier that the translocating domain needs to scale. The domain likely makes many failed attempts to cross it before reaching a stable observable state. These brief transitions occur within the conformational ensembles of the OFS and IFS.

Because the transport domain undergoes a concerted, rigid body movement, we applied LFER analysis to infer the structure of the TS in terms of the transport domain position along the trajectory from the OFS to the IFS. LFER analysis correlates changes of the TS free energy relative to the equilibrium end states (i.e., the height of the free energy barrier) to the changes of the free energy difference between the end states in response to perturbations, such as mutations or ligand additions or removals (Appendix Fig S14). The relative free energies of the TS and the end states are inferred from the forward and reverse reaction rate constants. If the TS resembles the OFS, mutations or ligands will change its free energy as much as the free energy of the OFS. If so, the change in free energy of the TS relative to the OFS,  $\Delta\Delta G_{OFS \rightarrow TS}^\ddagger$ , will be near zero. Thus, the height of the energy barrier crossed during the transition from the OFS to the IFS, and the corresponding forward rate constant,  $k_{OFS \rightarrow IFS}$ , will be unaltered. In contrast, the height of the free energy barrier crossed during the reverse transition from the IFS to the OFS,  $\Delta\Delta G_{IFS \rightarrow TS}^\ddagger$ , will change as much as the free energy of the IFS relative to the OFS, and the reverse rate constant,  $k_{IFS \rightarrow OFS}$ , will change accordingly (Appendix Fig S14). If, however, the TS resembles the IFS, the above relationships will be reversed. We will



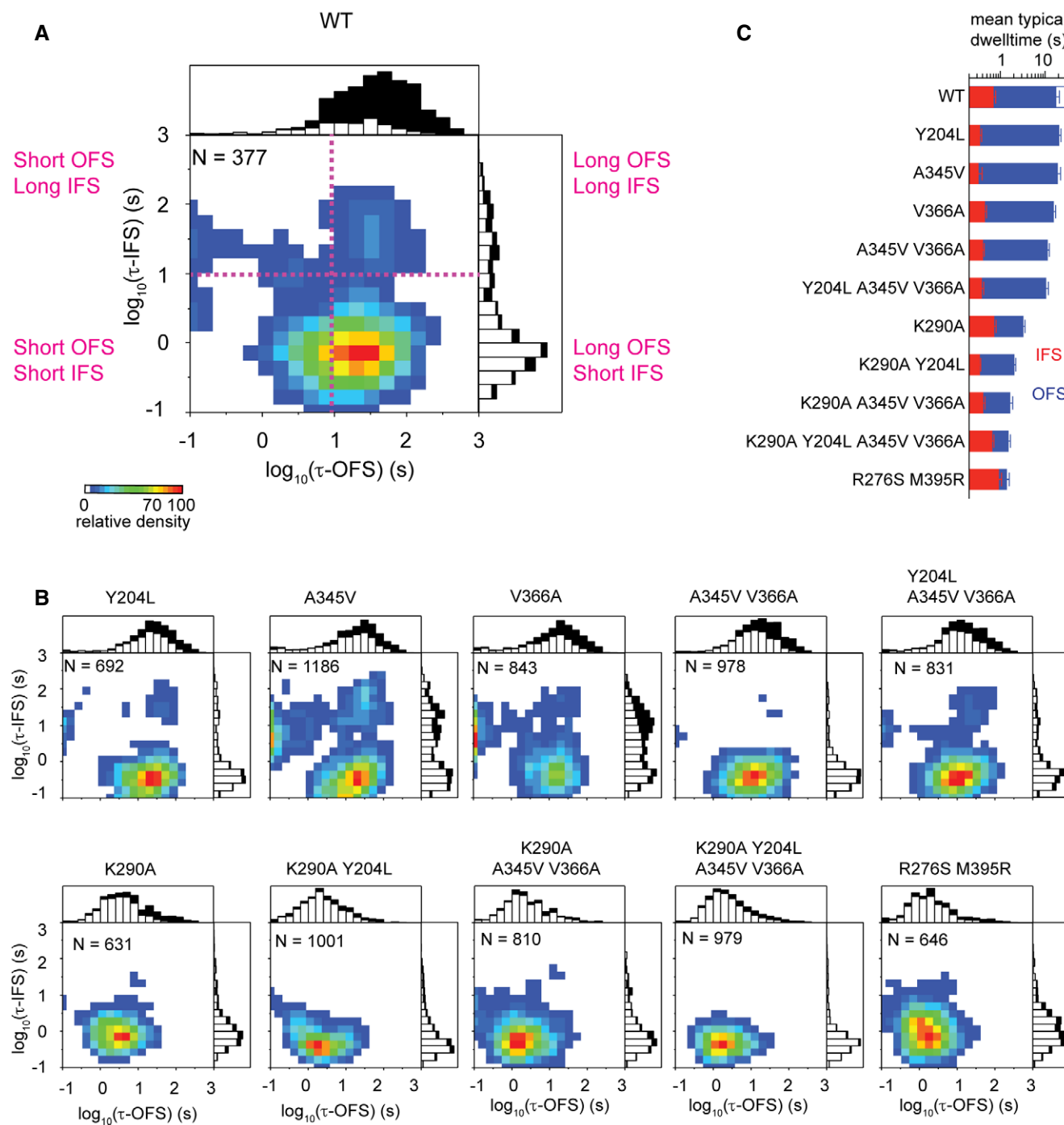


**Figure 5. Distributions of the OFS and the IFS lifetime pairs for individual molecules.**

A, B 2D histograms of lifetime pairs obtained for trajectories exhibiting single-exponential behavior.  $N$  is the number of traces used. Scale bar shows relative density normalized by the number of molecules. Above and to the right of each panel are stacked histograms of, respectively, the OFS and the IFS lifetimes of the analyzed molecules (open bars) and the photobleaching time of molecules showing no transitions (black bars). Data from three independent measurements were combined for presentation.

C The mean lifetimes of the molecules falling within 30% of the most populated bins of the 2D histograms (yellow to red; see Appendix Figure S11 for details). The open blue bar represents the calculated mean OFS lifetime for WT Gl<sub>TPH</sub> (see main text for details). Shown are means and standard errors of the mean of at least three independent measurements.

observe forward rate constants,  $k_{OFS \text{ to } IFS}$ , that change in response to the perturbations, and reverse rate constants,  $k_{IFS \text{ to } OFS}$ , that do not (Appendix Fig S14). Already a qualitative comparison of the smFRET recordings of WT  $\text{Glt}_{\text{ph}}$  in the absence and presence of the substrate and  $\text{Na}^+$  ions shows that the ligands mostly affect the duration of the OFS dwells ( $k_{OFS \text{ to } IFS}$ ). By contrast, the IFS dwells ( $k_{IFS \text{ to } OFS}$ ) are unchanged, hinting that the transition state might resemble the IFS (Appendix Fig S14).

Quantitatively, the linear relationship between the equilibrium and the TS free energies is expressed as follows (Evans & Polanyi, 1936; Leffler, 1953; Fersht & Sato, 2004):

$$\Delta\Delta G_{OFS \text{ to } TS}^{\ddagger} = \alpha \Delta\Delta G_{IFS}^{\ddagger} \text{ and } \Delta\Delta G_{IFS \text{ to } TS}^{\ddagger} = -(1-\alpha) \Delta\Delta G_{IFS}^{\ddagger} \quad (1)$$

where  $\Delta\Delta G_{IFS}^{\ddagger}$  is the change of the free energy of the IFS relative to the OFS. The Leffler  $\alpha$  approaches 0 or 1 when the TS resembles the OFS or the IFS, respectively (Fig 6A, *left and right*). Notably, if the transport domain in the TS assumes an intermediate position between the OFS and IFS, we will obtain different  $\alpha$ -values depending on the location of the perturbation (Fig 6A, *middle*). Mutations of residues involved in the same interactions in the TS as in the OFS or IFS will yield  $\alpha$ -values of 0 and 1, respectively. Mutating residues involved in interactions distinct from both will yield intermediate  $\alpha$ -values.

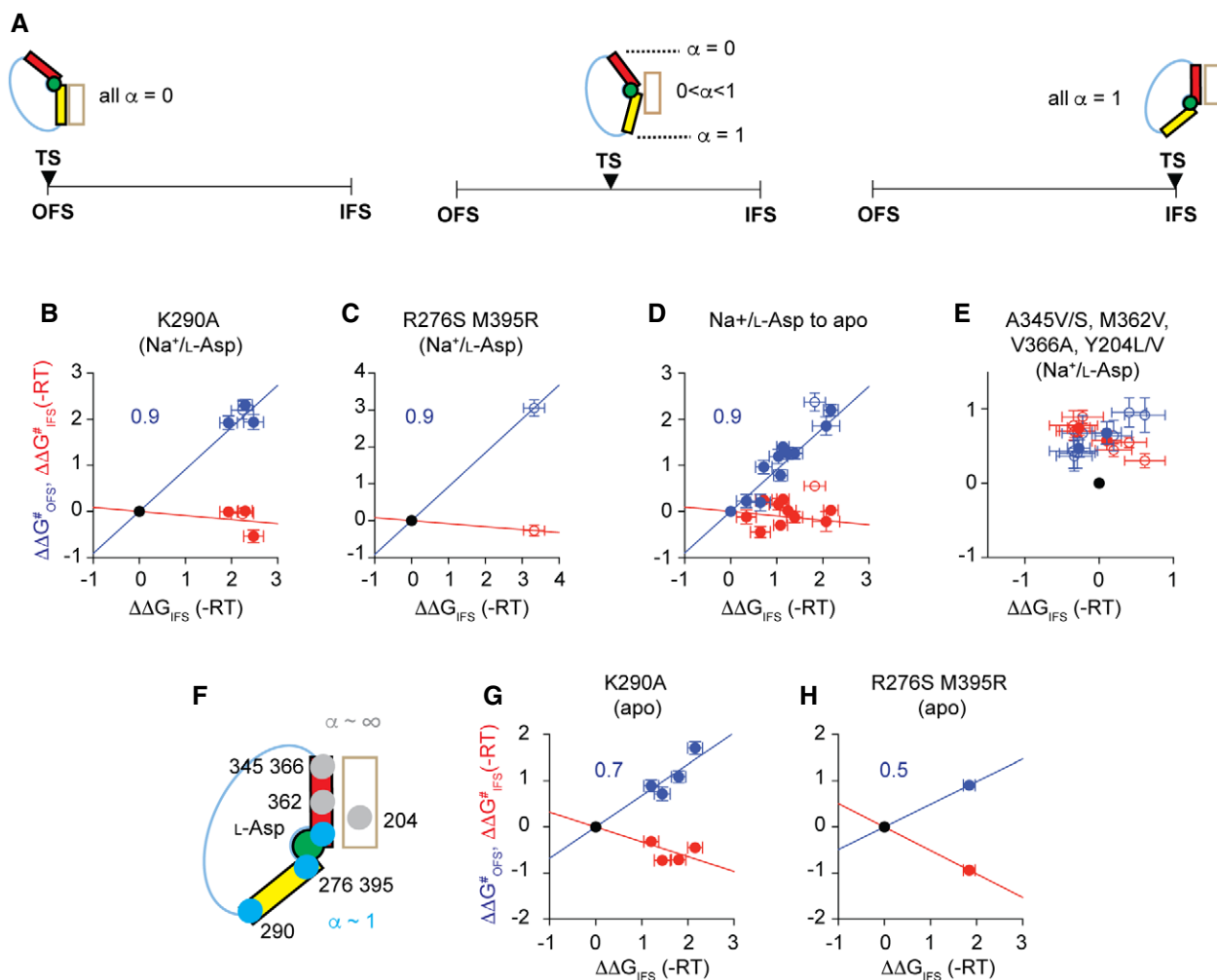


**Figure 6. Transition-state analysis**

A Schematic representation of the expected Leffler  $\alpha$ -values if the transition state is structurally similar to the OFS (left) or the IFS (right) or if it assumes an intermediate structure (middle). Color coding is the same as in Fig 1.

B–H LFER analysis. Free energy changes plotted in units of  $-RT$ . The activation free energies of the OFS-to-IFS transitions (blue) and the IFS-to-OFS transitions (red) were calculated by subtracting the energies of the reference states (black, at the origin) from the energies of the mutated protein variants. The K290A mutation was introduced into the WT, Y204L, A345V/V366A, and Y204/A345V/V366A backgrounds, either substrate-bound or apo (B and G, respectively). R276S/M395R and M362V mutations were introduced into the WT background (C, E, and H). For the transition from  $\text{Na}^+$ /L-Asp-bound to apo state, the free energies measured for the transporters in the presence of  $\text{Na}^+$  and L-Asp were subtracted from those measured for the apo transporters (D). Mutations at A345, V366, and Y204 sites and their combinations were introduced within the WT and K290A backgrounds (E). LFERs for the perturbations introduced within the WT background use back-calculated WT transition rates (see main text, open symbols). Data are averages over at least three independent repeats and errors are propagated from the standard error of the means in each replicate. (F) Schematic summary of sites where perturbations led to changes in the transition-state energy that scaled with the IFS energy (blue) and where they affected only the transition state (gray). See also Appendix Figs S11–S14.

Our complement of mutants allowed us to test the effects of perturbations along the scaffold-facing transport domain surface from the cytoplasmic base of HP1 to the extracellular base of HP2. For each, we estimated the rate constants,  $k_{OFS \text{ to } IFS}$  and  $k_{IFS \text{ to } OFS}$ , from the inverse of the mean OFS and IFS lifetimes of the molecules in the predominant dynamic mode (Fig 5B and Appendix Fig S12). First, we examined the effects of the K290A mutation at the base of HP1 (Fig 1A) introduced into the Y204L, A345V/V366A, and Y204L/A345V/V366A background mutants, because their characteristic OFS lifetimes were well determined (Fig 5B). We observed that the K290A mutation shortened the lifetimes of the OFS in these backgrounds (increased  $k_{OFS \text{ to } IFS}$ ) by  $9 \pm 2$  times on average but had little effect on the IFS lifetimes (Fig 5C). The free energies of the IFS and the TS decreased similarly by  $\sim 2$  RT relative to the OFS with the Leffler  $\alpha$  of  $0.91 \pm 0.08$  (Fig 6B). Therefore, we conclude that the salt bridge between K290 and E192 in the scaffold domain is already broken in the TS. The effect of the K290A mutation on WT Glt<sub>ph</sub> was similar to the other variants with only the OFS lifetime affected (Fig 5C). However, we were unable to measure the WT OFS lifetime directly because it was comparable to the fluorophore lifetime (Fig 5A). We, therefore, assumed that the mutation shortened the OFS lifetime to the same extent in the WT as in the other backgrounds and back-calculated the WT OFS lifetime to be  $\sim 30$  s from the lifetime of K290A Glt<sub>ph</sub>. We used this value in comparison with other mutations.

The R276S/M395R mutations at the HP1 tip (Fig 1A) also shifted the equilibrium toward the IFS, reducing the free energy of the TS and the IFS similarly, with the Leffler  $\alpha$  of 0.92 (Fig 6C). Furthermore, when we compared the translocation rates of all mutants in the presence of the saturating concentrations of Na<sup>+</sup> ions and L-Asp, and under apo conditions, we obtained mean Leffler  $\alpha$  of  $0.90 \pm 0.05$  (Fig 6D). R276 in HP1 and M395 in TM8 face the extracellular and cytoplasmic solutions in the OFS and IFS, respectively, poised to interact with different parts of the scaffold. Furthermore, HP2 undergoes a conformational change in the apo Glt<sub>ph</sub>, which alters the interface between the domains in the IFS, but not in the OFS (Verdon *et al*, 2014). Thus, our analysis suggests that HP1, HP2, and TM8 form similar interactions in the TS and the IFS. These findings are consistent with the transport domain completing most of the OFS-to-IFS movement before overcoming the principal barrier needed to achieve the IFS.

Finally, we examined mutations of A345, M362, and V366 residues on HP2 and Y204 in TM5 kink (Fig 1A). Surprisingly, multiple mutations at these sites led to the increases of both  $k_{OFS \text{ to } IFS}$  and  $k_{IFS \text{ to } OFS}$  within the WT or K290A backgrounds (Fig 6E). Increased rates of both forward and reverse reactions are a hallmark of mutations that stabilize the TS (Otzen, Itzhaki *et al*, 1994; Fersht & Sato, 2004). Thus, the TS structurally resembles the IFS but is sufficiently distinct so that mutations at Y204, A345, M362, and V366 sites affect the two states differentially (Fig 6F). Notably, when we constructed LFERs for the apo transporters, we observed Leffler  $\alpha$ -values of  $\sim 0.7$  and  $\sim 0.5$  for K290A and R276S/M395R mutants, respectively (Fig 6G and H). These results suggest that disrupting the domain interface in the OFS might become a kinetically more critical step when the barrier near the IFS diminishes (Fersht, Itzhaki *et al*, 1994; Fersht & Sato, 2004; Gopi, Paul *et al*, 2018).

## Discussion

To probe the structure of the rate limiting TS for transport domain movement in Glt<sub>ph</sub>, we first identified gain-of-function mutations by comparing sequences of homologues from hyperthermophilic, thermophilic, mesophilic, and psychrophilic bacteria. Functional assays and smFRET analyses of these mutants showed that the increased frequency of elevator transitions of the L-Asp-bound transport domain and the decreased L-Asp affinity lead to faster uptake rates. Single- and combination-HP2 mutants and the humanizing R276S/M395R mutant displayed increased dynamics and decreased L-Asp affinity. Thus, mutations in the transport domain can optimize multiple steps of the transport cycle at once, perhaps mimicking the natural evolutionary process.

Interestingly, the populations of the OFS and IFS in the HP2 mutants remained similar in the absence and presence of L-Asp and Na<sup>+</sup> ions (Appendix Table S5). Thus, their OFS and IFS have similar affinities for the substrate, as is also the case for the WT transporter (Reyes *et al*, 2013). Therefore, mutations in HP2 affect substrate binding similarly in the OFS and IFS and suggest that HP2 plays a similar gating role in the two states. Crystal structures of WT Glt<sub>ph</sub> in the IFS pictured HP2 immobilized at the domain interface (Reyes *et al*, 2009; Verdon & Boudker, 2012; Verdon *et al*, 2014). In contrast, structures of the R276S/M395R Glt<sub>ph</sub> mutant and the human homologue ASCT2 (Akyuz *et al*, 2015; Garaeva *et al*, 2019) showed so-called “unlocked” conformations, in which the transport domain leans away from the scaffold, providing space for HP2 to open. More recently, IFS structures of Na<sup>+</sup>-only-bound Glt<sub>ph</sub> and a closely related Glt<sub>TK</sub> showed that HP2 could open in these unlocked conformations, re-establishing interactions with scaffold and exposing the L-Asp-binding site (Arkhipova, Guskov *et al*, 2020; Wang & Boudker, 2020). Our results support this “one gate” model (Garaeva *et al*, 2019), whereby HP2 gates substrate binding in the OFS and the unlocked IFS. Collectively, these data suggest that the conformationally flexible HP2 (Boudker *et al*, 2007; Huang & Tajkhorshid, 2008; Shrivastava *et al*, 2008; Grazioso *et al*, 2012; Heinzelmann *et al*, 2013; Zomot & Bahar, 2013; Verdon *et al*, 2014) serves as a master regulator of substrate binding, translocation, release, and recycling of the apo transporter (Kortzak, Alleeva *et al*, 2019).

SmFRET recordings under equilibrium conditions in the presence of saturating Na<sup>+</sup> ions and L-Asp showed that the majority of Glt<sub>ph</sub> molecules resided in the OFS, consistent with earlier studies (Akyuz *et al*, 2013; Erkens *et al*, 2013; Georgieva *et al*, 2013; Hanelt *et al*, 2013; Akyuz *et al*, 2015; Ruan *et al*, 2017). Brief excursions into the IFS intersperse long OFS dwells. Long IFS dwells were also observed in some molecules, and sustained dynamics were seen in others. Overall, we found that the mean transition frequencies vary widely between the individual molecules in the WT and mutant transporters. Such behavior is best described in terms of multiple dynamic modes, whereby molecules show long-lasting kinetic differences. At present, the structural origins of the heterogeneity are not clear. It might arise from distinct protein conformations, but might also be due, for example, to distinct lipid interactions or other effects.

Linear free energy relationship analysis on nearly all introduced perturbations suggested that the TS for elevator movement structurally resembles the IFS. Hence, once the transport domain dislodges from the scaffold in the OFS, it might make multiple

attempts to reach the IFS before successfully crossing the high-energy barrier. Consistently, subtle packing mutations in HP2 affect both forward and reverse translocation rates, and altered domain interface was observed in the IFS structure of the dynamic R276S/M395R mutant (Akyuz *et al*, 2015). Thus, we hypothesize that exploring the local conformational space in the IFS-like TS to achieve a stable configuration of the domain interface is rate-limiting to the translocation process.

Placing TS within the structural vicinity of the IFS allows us to propose a strategy to develop small-molecule allosteric modulators for the transporter. We suggest that ligands binding at the domain interface with higher affinity for the IFS than for the OFS would also bind tighter to the TS. Such molecules would reduce the height of the energy barrier for the rate limiting elevator transition of the substrate-loaded domain and work as activators or positive allosteric modulators (PAMs) (Fig 7A). The degree to which PAMs can accelerate the transport cycle would depend on how much tighter they bind to the TS compared to the OFS and on the height of other,

unaffected barriers (Fig 7A and C). In contrast, molecules that bind tighter to the OFS would increase the height of the barrier and serve as negative allosteric modulators (NAMs) (Fig 7B).

PAMs of human EAATs could offer therapeutic opportunities to treat a plethora of conditions associated with glutamate-mediated excitotoxicity in the central nervous system (Fontana, 2015), but a rationale is lacking to aid their development. Similar to our most performant gain-of-function  $\text{Glt}_{\text{Ph}}$  mutant (Fig 7C), substrate binding and release are fast compared to the elevator movements in EAATs (Mim, Tao *et al*, 2007). However, in contrast to  $\text{Glt}_{\text{Ph}}$ , the return of the  $\text{K}^+$ -bound transport domain from the IFS to the OFS is the rate-limiting step (Grewer, Watzke *et al*, 2000). We stipulate that if the TS of this translocation reaction resembles the OFS structurally, small molecules that bind tighter to the OFS will act as PAMs. Recently developed compounds boost EAAT2 transport by  $\sim 2$ -fold (Kortagere, Mortensen *et al*, 2018; Falcucci, Wertz *et al*, 2019) and have features that agree with the concepts developed here. Indeed, the identified PAMs are thought to bind preferentially to the domain

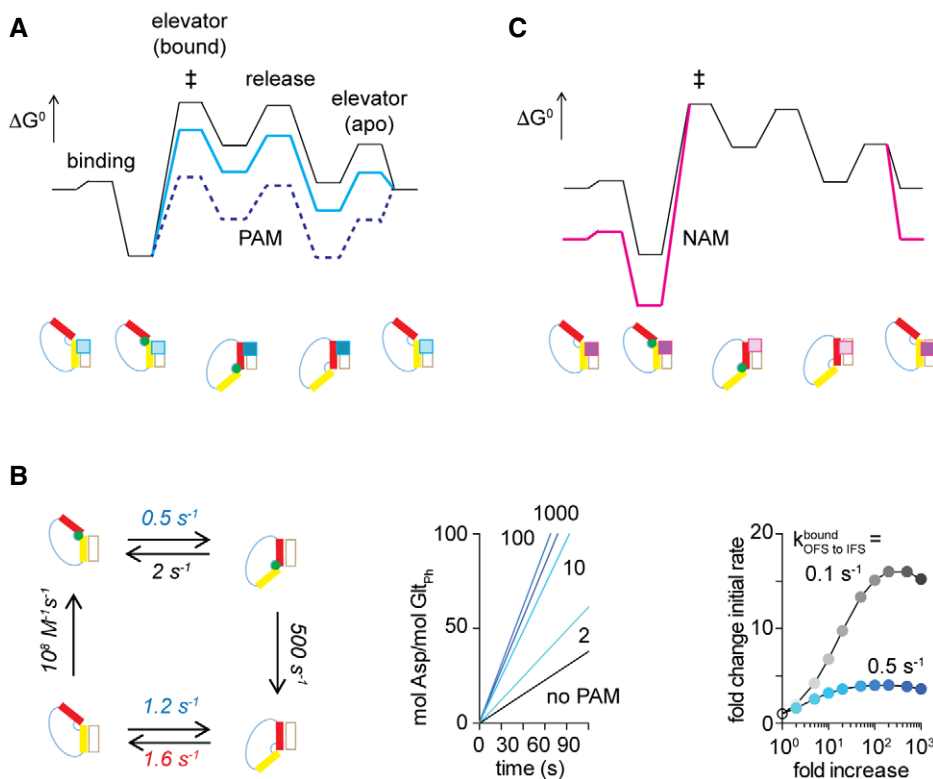


**Figure 7. Proposed model for allosteric modulation.**

- A, B A free energy diagram of the transport cycle (black) and its modulation (colors) by positive or negative allosteric modulators, PAMs (A) or NAMs (B), respectively. Cartoon representations of the low-energy states are below the diagrams and are colored as in Fig 1. The barrier heights are not to scale to the measured rates. Substrate binding to the apo OFS precedes isomerization into the IFS via the highest energy TS (‡) that structurally resembles the IFS. Substrate release and recycling into the OFS complete the cycle. PAMs, shown as squares in the cartoons of the states, bind with higher affinity to the IFS (dark cyan squares) than to the OFS (light cyan squares). Therefore, they stabilize all IFS-like states, including the TS, and smoothen the energy landscape (cyan line). PAMs that bind too tightly to the IFS may become inhibitory, as apo OFS becomes a high-energy state (dotted blue line). NAMs bind tighter to the OFS ((B), dark magenta squares), increase the ruggedness of the landscape (magenta line), and slow down transport.
- C Simulations of the transport rates in the absence and presence of PAMs. The left panel shows the transport cycle with the used rate constants (Materials and Methods). PAM effects were considered equal on both OFS-to-IFS isomerizations (blue rate constants). The acceleration of transport becomes rate-limited by the IFS-to-OFS isomerization of the apo transporter as PAM action increases OFS-to-IFS isomerizations (red rate constant). Middle and right panels show simulated uptake and fold increase in the initial rates, respectively, in the presence of PAMs that increase  $k_{\text{OFS to IFS}}^{\text{bound}}$  by the indicated number of folds (from cyan to dark blue). Simulations of cycles with  $k_{\text{OFS to IFS}}^{\text{bound}} = 0.1 \text{ s}^{-1}$  illustrate higher PAM potency (gray).

interface in the OFS (Kortagere *et al*, 2018; Falcucci *et al*, 2019). Moreover, chemically similar compounds act as activators or as inhibitors (Kortagere *et al*, 2018), as predicted by our model. However, further work is necessary to reveal the structural features of the TS for the IFS-to-OFS transitions in K<sup>+</sup>-bound EAATs.

Approximately 50 % of solute carriers are implicated in disease in humans, but only a few are drug targets (Rask-Andersen, Masuram *et al*, 2013). Our approach conceptualizes how the rate-limiting transition state of a transporter can be characterized structurally, informing on potential druggable sites to develop allosteric modulators, and provides a method to investigate the kinetic effects of post-translational modifications (Czuba *et al*, 2018). We anticipate that our methodology can be adapted to accelerate the expansion of therapeutic allosteric modulators in other protein systems with conformationally selective pockets, such as kinases (Hammam, Saez-Ayala *et al*, 2017; Zorba, Nguyen *et al*, 2019).

## Materials and Methods

### Bioinformatics analysis

The workflow of the bioinformatics approach is in Appendix Fig S1. Organism taxa, optimal growth temperatures, and temperature limits for growth were extracted from BacDive (Reimer, Vetcinova *et al*, 2019). Sequences of 20,000 prokaryotic homologues of Glt<sub>ph</sub> were collected using BLAST (Altschul, Madden *et al*, 1997) and aligned using MAFFT 7.0, applying the highest gap penalty (Katoh, Misawa *et al*, 2002). Multiple sequence alignments (MSA) were manually adjusted to optimize the alignment of the secondary structure elements and to remove sequences that were lacking one or more transmembrane helices. Sequences with over 90 % amino acid sequence identity were clustered using USEARCH (Edgar, 2010), and one random sequence per cluster was retained for subsequent analysis. Optimal growth temperatures and temperature limits were assigned to the sequences by matching GenInfo identifiers with genus and species annotations in BacDive database. Sequences without a match were excluded from further analysis. The remaining sequences were sorted into four temperature groups: psychrophiles (growth temperatures below 21°C), mesophiles (21°C–45°C), thermophiles (46°C–65°C), and hyperthermophiles (over 65°C). All temperature groups, except mesophiles, were manually sorted to exclude sequences originating from organisms with growth temperature ranges spanning more than two temperature groups. This process yielded 128, 5,811, 93, and 24 sequences from psychrophiles, mesophiles, thermophiles, and hyperthermophiles, respectively. The amino acid frequencies were calculated at each position in the MSA for all temperature groups using Prophecy (Rice, Longden *et al*, 2000) and using the Glt<sub>ph</sub> sequence as a reference. Combined frequencies were calculated for amino acids classified by their physicochemical properties (A + V, G, S + C+T + N+Q, P, D + E, H + M, Y + W, F + L+I, K + R) or side chain volumes (A + G+S, P + C+T + N+D, H + E+Q + V, Y + W+F, M + L+I + K+R). We used the outcomes of two-sample Kolmogorov–Smirnov tests to determine whether amino acid distributions at each position of the MSA were statistically different between pairs of temperature groups. Because no position showed significant distribution changes across all temperature groups, the results of every pairwise

comparison in the Kolmogorov–Smirnov test were weighted to reflect the temperature gap between the groups (i.e., multiplied by 3 for the comparison between the hyperthermophiles and psychrophiles, and 2 for thermophiles and psychrophiles). A positive value of the sum of the weighted values (global difference score) for a given position in the MSA indicates a change of the amino acid distribution correlated to the optimal growth temperature. Among the amino acids with positive global difference score, mutation sites were selected according to the following criteria: (i) Their side chains were not exposed to either aqueous solution or lipid bilayer; (ii) they were in well-conserved regions; and (iii) they were not directly coordinating L-Asp or Na<sup>+</sup> ions. Additional residues in these areas were chosen to perturb packing interactions (I85, L303, T322, I341, and M362). Differences in the crystal structures of WT Glt<sub>ph</sub> in the OFS and the IFS were used to guide mutagenesis of several residues in the interdomain hinges (A70, P75, Q220, H223, G226, and E227) and TM2/5 kink (D48 and Y204). Glt<sub>ph</sub> residues were mostly mutated to those prevalent in mesophiles or psychrophiles, in most cases producing conservative mutations that lead to subtle volume changes or the removal of hydrogen bonds.

### Mutagenesis, protein expression, purification, and labeling

Amino acid substitutions were introduced by site-directed mutagenesis (*Stratagene*) in a Glt<sub>ph</sub> variant with seven non-conserved surface-exposed residues replaced with histidines to increase expression yields (referred to as wild-type; Yernool *et al*, 2004). For smFRET microscopy, substitutions were introduced within the Glt<sub>ph</sub> variant with additional C321A and N378C mutations, as previously described (Akyuz *et al*, 2013). Constructs were cloned in-frame into pBAD24 vector with a C-terminal thrombin cleavage site followed by octa-histidine tag as described previously (Yernool *et al*, 2004) and verified by DNA sequencing. Plasmids were transformed into *E. coli* strain DH10B (*Invitrogen*), and protein expression was induced for 3 h at 37°C by 0.1 % arabinose. Glt<sub>ph</sub> was purified from cell membranes, as described previously (Yernool *et al*, 2004). Briefly, membranes were solubilized in a buffer containing 20 mM Hepes/Tris, pH 7.4, 200 mM NaCl, 1 mM L-Asp, and 40 mM *n*-dodecyl-β-D-maltopyranoside (DDM, *Anatrace*). Insoluble material was removed by ultracentrifugation at 100,000 g for 1 h at 4°C. Solubilized transporters were bound to nickel agarose (*Qiagen*) for 2 h at 4°C. The resin was washed in the same buffer containing 1 mM DDM and 40 mM imidazole and proteins eluted with 250 mM imidazole. The tag was removed by overnight cleavage with thrombin at room temperature using 10 units per mg Glt<sub>ph</sub>. The proteins were further purified by size-exclusion chromatography on a Superdex 200 Increase 10/300 GL column in buffers of various compositions: 10 mM Hepes/Tris, pH 7.4, 200 mM NaCl, 1 mM L-Asp, and 7 mM *n*-decyl-β-D-maltopyranoside (DM, *Anatrace*) for transport assays; 10 mM Hepes/Tris, pH 7.4, 50 mM NaCl, 0.1 mM L-Asp, and 5 mM DM for crystallization; 10 mM Hepes/Tris, pH 7.4, 1 mM NaCl, 200 mM choline chloride, and 1 mM DDM for binding assays; and 10 mM Hepes/Tris, pH 7.4, 200 mM NaCl, 1 mM L-Asp, and 1 mM DDM for smFRET microscopy. When Glt<sub>ph</sub> proteins were purified for smFRET microscopy, all buffers were supplemented with 0.1 mM Tris(2-carboxyethyl)phosphine (TCEP). Glt<sub>ph</sub> purity was confirmed by SDS–PAGE, followed by Coomassie Brilliant Blue R-

250 staining. For smFRET studies, purified Glt<sub>ph</sub> variants at 40 μM were labeled randomly with maleimide-activated LD555P-MAL and LD655-MAL dyes (Altman *et al*, 2012; Zheng *et al*, 2014) and biotin-PEG<sub>11</sub> (Thermo Fisher Scientific) at final concentrations of 50, 100, and 25 μM, respectively, as previously described (Akyuz *et al*, 2013). Labeling efficiency was determined by spectrophotometry using extinction coefficients of 57,400, 150,000, and 250,000 M<sup>-1</sup> cm<sup>-1</sup> for Glt<sub>ph</sub>, LD555P-MAL, and LD655-MAL, respectively. Excess dyes were removed on a PD MiniTrap Sephadex G-25 desalting column (GE Healthcare).

### L-Asp binding assays

Fluorescence-binding assays were performed as described previously (Verdon *et al*, 2014). Briefly, Glt<sub>ph</sub> was diluted to a final concentration of 2 μM in buffer containing 20 mM Hepes/Tris, pH 7.4, 200 mM choline chloride, 0.4 mM DDM, and 0.4 nM RH421 dye (Invitrogen) supplemented with 1 or 10 mM NaCl, as indicated. RH421 was excited at 532 nm, and emission was measured at 628 nm at 25 °C using a QuantaMaster fluorometer equipped with a magnetic stirrer (Photon International Technologies). Fluorescence changes induced by additions of L-Asp aliquots were monitored until stable for ~100 s, corrected for dilution, and normalized to the maximal fluorescence change. Binding isotherms were plotted and fitted to the Hill equation using Prism (GraphPad). All measurements were performed in triplicate.

### Glt<sub>ph</sub> reconstitution into liposomes and transport assays

Glt<sub>ph</sub> variants were reconstituted into liposomes as described previously (Yernool *et al*, 2003). Liposomes were prepared using *E. coli* polar lipid extract, egg yolk L-α-phosphatidylcholine, and 1,2-dioleoyl-sn-glycero-3-phosphoethanolamine-N-(lissamine rhodamine B sulfonyl) (Avanti Polar Lipids) in a 3,000:1,000:1 (w/w/w) ratio. The dried lipid films were hydrated in buffer containing 20 mM Hepes/Tris, pH 7.4, 200 mM KCl, 100 mM choline chloride at a final concentration of 70 mM lipid by repeated freeze–thaw cycles. Liposomes were extruded through polycarbonate filters with a pore size of 400 nm (Avanti Polar Lipids) and destabilized with Triton X-100 (Sigma) at a detergent-to-lipid ratio of 0.5:1 (w/w). Glt<sub>ph</sub> variants were added at final protein-to-lipid ratios of 1:2000 (w/w) and incubated for 30 min at 22°C. Detergents were removed by repeated incubations with Bio-Beads SM-2 (Bio-Rad). Liposomes were concentrated by ultracentrifugation at 100,000 g for 1 h at 4°C, subjected to three freeze–thaw cycles, and extruded through 400-nm polycarbonate filters (Avanti Polar Lipids). To initiate transport, liposomes were diluted 100-fold into a buffer containing 20 mM Hepes/Tris, pH 7.4, 200 mM KCl, 100 mM NaCl, 0.5 μM valinomycin, and variable concentrations of <sup>3</sup>H-L-Asp (aspartic acid, L-[2,3-<sup>3</sup>H], PerkinElmer). When necessary, the reaction mixtures were supplemented with cold L-Asp. At appropriate time points, 200 μl aliquots were removed and diluted into ice-cold quench buffer containing 20 mM Hepes/Tris, pH 7.4, 200 mM LiCl, and 100 mM choline chloride, followed by rapid filtration using 0.22-μm nitrocellulose filters (Whatman). Filters were washed three times using a total of 8 ml quench buffer. The retained radioactivity was measured by scintillation counting in a LS-6500 counter (Beckman Coulter). To determine L-Asp K<sub>M</sub>, concentration dependences were

measured using 1-min incubation to achieve robust signals for all variants. Uptake time courses were measured at concentrations of L-Asp of 5 times over K<sub>M</sub> for 90 s. All uptake experiments were performed at 34°C. The background was determined in the reaction buffer lacking NaCl and subtracted from the measurements. The proteoliposome concentration was determined by measuring rhodamine fluorescence using excitation and emission wavelengths of 530 and 590 nm, respectively. The protein concentration was estimated by assuming similar reconstitution efficiencies for all Glt<sub>ph</sub> variants. The amount of L-Asp uptake was normalized per Glt<sub>ph</sub> monomer. Dose–response curves and initial time courses were plotted and fitted in Prism (GraphPad).

### Crystallography

Purified Y204L/A345V/V366A Glt<sub>ph</sub> mutant was concentrated to 3 mg/ml. Protein was mixed 1:1 with a reservoir solution containing 100 mM potassium citrate pH 4.4–5 and 12–17% PEG 400. The protein was crystallized at 4°C by hanging-drop vapor diffusion method. Crystals were cryo-protected in reservoir solution supplemented with 30–35% PEG 400. Diffraction data were collected at Advanced Light Source beamline 8.2.2. Diffraction data were indexed, integrated, and scaled using HKL2000 (Otwinowski & Minor, 1997). Initial phases were determined by molecular replacement in Phaser (McCoy, Grosse-Kunstleve *et al*, 2007) using 2NWX as the search model. The model was optimized by iterative rounds of refinement and rebuilding in Phenix (Adams, Grosse-Kunstleve *et al*, 2002) and Coot (Emsley & Cowtan, 2004). Strict non-crystallographic threefold symmetry was applied during refinement.

### smFRET microscopy and data analysis

Glt<sub>ph</sub> was reconstituted into liposomes as above with modifications. The 1,2-dioleoyl-sn-glycero-3-phosphoethanolamine-N-(lissamine rhodamine B sulfonyl) was omitted, and the lipid film was hydrated in buffer containing 20 mM Hepes/Tris, pH 7.4, and 200 mM KCl. Glt<sub>ph</sub> was added at a final protein-to-lipid ratio of 1:1,000 (w/w) to maximize the number of liposomes containing one trimer. Liposomes were extruded through 100-nm polycarbonate filters (Avanti Polar Lipids). To replace internal liposome buffer, vesicles were subjected to three rounds of the following procedure. Proteoliposomes were pelleted by centrifugation for 40 min at 100,000 g at 4°C, resuspended in buffer containing 20 mM Hepes/Tris, pH 7.4, 200 mM NaCl or 20 mM Hepes/Tris, pH 7.4, 200 mM NaCl, and 0.1 mM L-Asp, as required, and subjected to a freeze–thaw cycle.

All smFRET experiments were performed on a home-built prism-based total internal reflection fluorescence (TIRF) microscope constructed around a Nikon Eclipse Ti inverted microscope using passivated microfluidic imaging chambers (Munro, Altman *et al*, 2007; Juetten *et al*, 2016). The samples were illuminated with a 532-nm laser (Laser Quantum). LD555P and LD655 fluorescence signals were separated using a T635lpxr dichroic filter (Chroma) mounted in a MultiCam apparatus (Cairn). Imaging data were acquired using home-written acquisition software and scientific complementary metal–oxide–semiconductor (sCMOS) cameras (Hamamatsu).

Labeled Glt<sub>ph</sub> variants in proteoliposomes were surface-immobilized via a biotin–streptavidin bridge on PEG-passivated microfluidic imaging chambers functionalized with streptavidin. Imaging experiments were performed in 20 mM Hepes/Tris buffers at pH 7.4 containing 5 mM β-mercaptoethanol and an oxygen scavenger system comprised of 1 U/ml glucose oxidase (*Sigma*), 8 U/ml catalase (*Sigma*), and 0.1 % glucose (*Sigma*). Experiments under symmetric apo conditions were performed in buffer supplemented with 200 mM KCl using proteoliposomes loaded with buffer containing 200 mM KCl. Under non-equilibrium transport conditions, imaging buffer was supplemented with 200 mM NaCl and 0.1 mM L-Asp. For symmetric saturating Na<sup>+</sup>/L-Asp conditions, the internal liposome and imaging buffers contained 200 mM NaCl and 0.1 mM L-Asp. To inhibit protein dynamics, liposomes containing 200 mM NaCl were incubated in imaging buffer containing 200 mM NaCl and 10 mM D,L-TBOA. Data were collected using 10- or 100-ms averaging time. Single-molecule fluorescence trajectories were selected for analysis in SPARTAN (Juetter *et al*, 2016) implemented in MATLAB (*MathWorks*). Trajectories were corrected for spectral bleed-through from donor to acceptor channel by subtracting a fraction of the donor intensity from the acceptor (0.168). Acquired traces were selected for analysis using the following criteria: a single catastrophic photobleaching event, ascertaining Glt<sub>ph</sub> labeling with a single LD555P-MAL and LD655-MAL label; over 10:1 signal-to-background noise ratio; over 5:1 signal-to-signal noise ratio; FRET lifetime of at least 5 s; and a maximum of 1 donor blink per trajectory. FRET trajectories were calculated from LD555P and LD655 intensities,  $I_D$  and  $I_A$ , respectively, using  $E_{FRET} = I_A/(I_D + I_A)$ . Population contour plots were constructed by superimposing  $E_{FRET}$  from individual trajectories and fitted to Gaussian distributions in Prism (*GraphPad*). Dwell-time distributions and transition frequencies were obtained by idealizing  $E_{FRET}$  trajectories in SPARTAN (Juetter *et al*, 2016). State survival plots and dwell-time histograms were fitted to double or triple exponentials and the probability density functions (Sigworth & Sine, 1987), respectively. Analyses of transition frequencies, dwell times, and survival plots for individual trajectories were performed using custom-made scripts implemented in MATLAB (*MathWorks*). State survival plots of individual trajectories were fitted to single exponentials or double exponentials if R<sup>2</sup> increased by at least 5 %, and the time constants differed at least fivefold. Fits were only performed when traces contained at least 5 visits to the OFS or the IFS. Mean dwell times were used otherwise. For illustration purposes, state survival plots of selected molecules were refitted in Prism (*GraphPad*). 2D histograms were generated in Origin (*OriginLab*). The autocorrelation coefficients  $R(t/o)$  of the dwell durations as functions of the number of consecutive state visits were calculated as  $R(t/o) = \frac{\sum_i (\tau_i - \langle \tau \rangle) (\tau_{i+t/o} - \langle \tau \rangle)}{\sum_i (\tau_i - \langle \tau \rangle)^2}$ , where  $t/o$  are the number turnovers,  $\tau_i$  the dwell lengths, and  $\langle \tau \rangle$  the average dwell time over the trajectory (Lu *et al*, 1998). Each experiment was performed at least in triplicate using independent protein reconstitutions and buffer preparations. In each experiment, a minimum of 400 molecules was selected.

### Transition-state analysis

LFER analysis builds on observations from reaction chemistry (Evans & Polanyi, 1936; Leffler, 1953), which correlate changes of the rate constants with changes of the equilibrium constant

upon perturbations of the start and end equilibrium states. Here, the free energy change of the transition state,  $\Delta G^\ddagger$ , is expected to fall between the free energy changes of the equilibrium end states, the OFS and the IFS, following perturbations (Leffler, 1953):

$$\Delta G^\ddagger = \alpha \Delta G_{IFS} + (1 - \alpha) \Delta G_{OFS} \quad (2)$$

where  $\alpha$  varies between 0 and 1. Equation 2 can be rewritten to express the energy changes relative to the OFS:

$$\Delta \Delta G_{OFS \rightarrow IFS}^\ddagger = \alpha \Delta \Delta G_{IFS} \quad (3)$$

where  $\Delta \Delta G_{OFS \rightarrow IFS}^\ddagger$  is the activation energy of the transition from the OFS to the IFS. The activation energy of the reverse reaction can be expressed similarly:

$$\Delta \Delta G_{IFS \rightarrow OFS}^\ddagger = -(1 - \alpha) \Delta \Delta G_{IFS} \quad (4)$$

The equilibrium free energy change is calculated from equilibrium constants before and after the perturbation,  $K_R$  and  $K_P$  (where  $R$  and  $P$  stand for “reference” and “perturbation”), respectively:

$$\Delta \Delta G_{IFS} = -RT \ln \left( \frac{K_P}{K_R} \right) \quad (5)$$

The equilibrium constants are obtained as ratios of the forward and reverse rate constants  $k_{OFS \rightarrow IFS}$  and  $k_{IFS \rightarrow OFS}$  measured before and after the perturbation. The transition-state energy changes can be approximated as in Kramers theory assuming that the transition mechanism (i.e., the shape of the energy barrier) is not altered by the perturbation (Kramers, 1940):

$$\Delta \Delta G_{OFS \rightarrow IFS}^\ddagger = -RT \ln \left( \frac{k_{OFS \rightarrow IFS, P}}{k_{OFS \rightarrow IFS, R}} \right) \quad (6)$$

$\Delta \Delta G_{IFS \rightarrow OFS}^\ddagger$  is calculated in an analogous manner from the reverse reaction rates.

### Kinetic modeling of the transport cycle

The transport cycle for WT Glt<sub>ph</sub> was simulated in COPASI (Hoops, Sahle *et al*, 2006). A two-compartment system was created to reflect external and internal proteoliposome space. The initial conditions were 200 mM Na<sup>+</sup> and 1 mM L-Asp in the external space with all transporters in the apo state and the fraction of the OFS at 0.6. External substrate binding and internal substrate release were approximated as irreversible. External substrate binding was arbitrarily set to 10<sup>8</sup> M<sup>-4</sup>s<sup>-1</sup>, while internal release was set to an estimated value of 500 s<sup>-1</sup> (Oh & Boudker, 2018). Rate constants for the conformational changes were estimated from the mean lifetimes of “typical” Y204L/K290A/A345V/V366A Glt<sub>ph</sub> molecules analyzed by smFRET and set at  $k_{OFS \rightarrow IFS, apo} = 1.2 \text{ s}^{-1}$ ,  $k_{IFS \rightarrow OFS, apo} = 1.6 \text{ s}^{-1}$ ,  $k_{OFS \rightarrow IFS, bound} = 0.5 \text{ s}^{-1}$ , and  $k_{IFS \rightarrow OFS, bound} = 2.0 \text{ s}^{-1}$ . The effect of a positive allosteric modulator on  $k_{OFS \rightarrow IFS, bound}$  and  $k_{OFS \rightarrow IFS, apo}$  was considered the same, and the increase in transport rate was simulated for 2-, 5-, 10-, 20-, 50-, 100-, 200-, 500-, and 1,000-fold increases of  $k_{OFS \rightarrow IFS, bound}$  and  $k_{OFS \rightarrow IFS, apo}$ . Time courses were simulated over 1,000 s.

**Statistical analysis**

All data reflect the means and standard deviation over at least three replicates. The standard error of the mean was used for the typical OFS and IFS lifetimes.

**Data availability**

The structure of Y204L A345V V366A Gl<sub>TPH</sub> has been submitted to the PDB (accession code: 6V8G).

**Expanded View** for this article is available online.

**Acknowledgements**

We thank Roger Altman for preparation of smFRET chambers, Zhou Zhou for dye formulations, Eva Fortea and Emma Garst for assistance with crystallization trials, and Lucy Skrabanek for R scripts used in bioinformatics sequence analysis. We thank Julia Chamot-Rooke for continued support. We are grateful for the support of NINDS (R37NS085318 to O.B. and S.C.B.) and AHA (19PRE34380215 to H.D.C.). This project has received funding from the European Union's Horizon 2020 research and innovation program under the Marie Skłodowska-Curie grant agreement MEMDYN No 660083 (to G.H.M.H.).

**Author contributions**

GHHM and OB conceived the study. GHHM acquired the data. GHHM, DC, XW, and OB analyzed the data. OB and SCB collected the resources. GHHM and OB wrote the manuscript with input from all other authors.

**Conflict of Interest**

The authors declare that they have no conflict of interest.

**References**

- Adams PD, Grosse-Kunstleve RW, Hung LW, Ioerger TR, McCoy AJ, Moriarty NW, Read RJ, Sacchettini JC, Sauter NK, Terwilliger TC (2002) PHENIX: building new software for automated crystallographic structure determination. *Acta Crystallogr D Biol Crystallogr* 58: 1948–1954
- Akanuma S, Bessho M, Kimura H, Furukawa R, Yokobori SI, Yamagishi A (2019) Establishment of mesophilic-like catalytic properties in a thermophilic enzyme without affecting its thermal stability. *Sci Rep* 9: 9346
- Akyuz N, Altman RB, Blanchard SC, Boudker O (2013) Transport dynamics in a glutamate transporter homologue. *Nature* 502: 114–118
- Akyuz N, Georgieva ER, Zhou Z, Stolzenberg S, Cuendet MA, Khelashvili G, Altman RB, Terry DS, Freed JH, Weinstein H et al (2015) Transport domain unlocking sets the uptake rate of an aspartate transporter. *Nature* 518: 68–73
- Altman RB, Zheng Q, Zhou Z, Terry DS, Warren JD, Blanchard SC (2012) Enhanced photostability of cyanine fluorophores across the visible spectrum. *Nat Methods* 9: 428–429
- Altschul SF, Madden TL, Schaffer AA, Zhang J, Zhang Z, Miller W, Lipman DJ (1997) Gapped BLAST and PSI-BLAST: a new generation of protein database search programs. *Nucleic Acids Res* 25: 3389–3402
- Arkhipova V, Guskov A, Slotboom DJ (2020) Structural ensemble of a glutamate transporter homologue in lipid nanodisc environment. *Nat Commun* 11: 998
- Arkhipova V, Trinco G, Ettema TW, Jensen S, Slotboom DJ, Guskov A (2019) Binding and transport of D-aspartate by the glutamate transporter homolog GlTk. *Elife* 8, e45286.
- Auerbach A (2003) Life at the top: the transition state of AChR gating. *Sci Signal* 2003: re11
- Auerbach A, Lingle CJ (1986) Heterogeneous kinetic properties of acetylcholine receptor channels in *Xenopus myocytes*. *J Physiol* 378: 119–140
- Blatz AL, Magleby KL (1986) Correcting single channel data for missed events. *Biophys J* 49: 967–980
- Boudker O, Ryan RM, Yernool D, Shimamoto K, Gouxau E (2007) Coupling substrate and ion binding to extracellular gate of a sodium-dependent aspartate transporter. *Nature* 445: 387–393
- Canul-Tec JC, Assal R, Cirri E, Legrand P, Brier S, Chamot-Rooke J, Reyes N (2017) Structure and allosteric inhibition of excitatory amino acid transporter 1. *Nature* 544: 446–451
- Cesar-Razquin A, Snijder B, Frappier-Brinton T, Isserlin R, Gyimesi G, Bai X, Reithmeier RA, Hepworth D, Hediger MA, Edwards AM et al (2015) A call for systematic research on solute carriers. *Cell* 162: 478–487
- Cheng MH, Kaya C, Bahar I (2018) Quantitative assessment of the energetics of dopamine translocation by human dopamine transporter. *J Phys Chem B* 122: 5336–5346
- Chung HS, McHale K, Louis JM, Eaton WA (2012) Single-molecule fluorescence experiments determine protein folding transition path times. *Science* 335: 981–984
- Chung HS, Piana-Agostinetti S, Shaw DE, Eaton WA (2015) Structural origin of slow diffusion in protein folding. *Science* 349: 1504–1510
- Ciftci D, Huysmans GHM, Wang X, He C, Terry D, Zhou Z, Fitzgerald G, Blanchard SC, Boudker O (2020) Single-molecule transport kinetics of a glutamate transporter homolog shows static disorder. *Sci Adv* 6: eaaz1949
- Compton EL, Taylor EM, Mindell JA (2010) The 3–4 loop of an archaeal glutamate transporter homolog experiences ligand-induced structural changes and is essential for transport. *Proc Natl Acad Sci USA* 107: 12840–12845
- Crisman TJ, Qu S, Kanner BI, Forrest LR (2009) Inward-facing conformation of glutamate transporters as revealed by their inverted-topology structural repeats. *Proc Natl Acad Sci USA* 106: 20752–20757
- Curnow P, Booth PJ (2009) The transition state for integral membrane protein folding. *Proc Natl Acad Sci USA* 106: 773–778
- Czuba LC, Hillgren KM, Swaan PW (2018) Post-translational modifications of transporters. *Pharmacol Ther* 192: 88–99
- Dick M, Weiergraber OH, Classen T, Bisterfeld C, Bramski J, Gohlke H, Pietruszka J (2016) Trading off stability against activity in extremophilic aldolases. *Sci Rep* 6: 17908
- Drew D, Boudker O (2016) Shared Molecular Mechanisms of Membrane Transporters. *Annu Rev Biochem* 85: 543–572
- Edgar RC (2010) Search and clustering orders of magnitude faster than BLAST. *Bioinformatics* 26: 2460–2461
- Elias M, Wieczorek G, Rosenne S, Tawfik DS (2014) The universality of enzymatic rate-temperature dependency. *Trends Biochem Sci* 39: 1–7
- Emsley P, Cowtan K (2004) Coot: model-building tools for molecular graphics. *Acta Crystallogr D Biol Crystallogr* 60: 2126–2132
- Erkens GB, Hanelt I, Goudsmits JM, Slotboom DJ, van Oijen AM (2013) Unsynchronised subunit motion in single trimeric sodium-coupled aspartate transporters. *Nature* 502: 119–123
- Espinoza-Fonseca LM, Thomas DD (2011) Atomic-level characterization of the activation mechanism of SERCA by calcium. *PLoS One* 6: e26936



- Evans MG, Polanyi M (1936) Further considerations on the thermodynamics of chemical equilibria and reaction rates. *Trans Faraday Soc* 32: 1333–1360
- Falcucci RM, Wertz R, Green JL, Meucci O, Salvino J, Fontana ACK (2019) Novel positive allosteric modulators of glutamate transport have neuroprotective properties in an in vitro excitotoxic model. *ACS Chem Neurosci* 10: 3437–3453
- Feller G (2010) Protein stability and enzyme activity at extreme biological temperatures. *J Phys Condens Matter* 22: 323101
- Fersht AR, Itzhaki LS, elMasry NF, Matthews JM, Otzen DE (1994) Single versus parallel pathways of protein folding and fractional formation of structure in the transition state. *Proc Natl Acad Sci USA* 91: 10426–10429
- Fersht AR, Sato S (2004) Phi-value analysis and the nature of protein-folding transition states. *Proc Natl Acad Sci USA* 101: 7976–7981
- Fersht AR, Wells TN (1991) Linear free energy relationships in enzyme binding interactions studied by protein engineering. *Protein Eng* 4: 229–231
- Fontana AC (2015) Current approaches to enhance glutamate transporter function and expression. *J Neurochem* 134: 982–1007
- Gaillard I, Slotboom DJ, Knol J, Lolkema JS, Konings WN (1996) Purification and reconstitution of the glutamate carrier GltT of the thermophilic bacterium *Bacillus stearothermophilus*. *Biochemistry* 35: 6150–6156
- Garaeva AA, Guskov A, Slotboom DJ, Paulino C (2019) A one-gate elevator mechanism for the human neutral amino acid transporter ASCT2. *Nat Commun* 10: 3427
- Georgieva ER, Borbat PP, Ginter C, Freed JH, Boudker O (2013) Conformational ensemble of the sodium-coupled aspartate transporter. *Nat Struct Mol Biol* 20: 215–221
- Gopi S, Paul S, Ranu S, Naganathan AN (2018) Extracting the hidden distributions underlying the mean transition state structures in protein folding. *J Phys Chem Lett* 9: 1771–1777
- Grazioso G, Limongelli V, Branduardi D, Novellino E, De Micheli C, Cavalli A, Parrinello M (2012) Investigating the mechanism of substrate uptake and release in the glutamate transporter homologue Glt(Ph) through metadynamics simulations. *J Am Chem Soc* 134: 453–463
- Grewer C, Watzke N, Wiessner M, Rauert T (2000) Glutamate translocation of the neuronal glutamate transporter EAAC1 occurs within milliseconds. *Proc Natl Acad Sci USA* 97: 9706–9711
- Groeneveld M, Slotboom DJ (2010) Na(+):aspartate coupling stoichiometry in the glutamate transporter homologue Glt(Ph). *Biochemistry* 49: 3511–3513
- Grosman C, Zhou M, Auerbach A (2000) Mapping the conformational wave of acetylcholine receptor channel gating. *Nature* 403: 773–776
- Gur M, Zomot E, Bahar I (2013) Global motions exhibited by proteins in micro- to milliseconds simulations concur with anisotropic network model predictions. *J Chem Phys* 139: 121912
- Gur M, Zomot E, Cheng MH, Bahar I (2015) Energy landscape of LeuT from molecular simulations. *J Chem Phys* 143: 243134
- Guskov A, Jensen S, Faustino I, Marrink SJ, Slotboom DJ (2016) Coupled binding mechanism of three sodium ions and aspartate in the glutamate transporter homologue GltTk. *Nat Commun* 7: 13420
- Hammam K, Saez-Ayala M, Rebuffet E, Gros L, Lopez S, Hajem B, Humbert M, Baudalet E, Audebert S, Betzi S et al (2017) Dual protein kinase and nucleoside kinase modulators for rationally designed polypharmacology. *Nat Commun* 8: 1420
- Hanelt I, Jensen S, Wunnicke D, Slotboom DJ (2015) Low affinity and slow Na<sup>+</sup> binding precedes high affinity aspartate binding in the secondary-active transporter GltPh. *J Biol Chem* 290: 15962–15972
- Hanelt I, Wunnicke D, Bordignon E, Steinhoff HJ, Slotboom DJ (2013) Conformational heterogeneity of the aspartate transporter Glt(Ph). *Nat Struct Mol Biol* 20: 210–214
- Heinzelmann G, Bastug T, Kuyucak S (2013) Mechanism and energetics of ligand release in the aspartate transporter GltPh. *J Phys Chem B* 117: 5486–5496
- Hollfelder F, Herschlag D (1995) The nature of the transition state for enzyme-catalyzed phosphoryl transfer. Hydrolysis of O-aryl phosphorothioates by alkaline phosphatase. *Biochemistry* 34: 12255–12264
- Hoops S, Sahle S, Gauges R, Lee C, Pahle J, Simus N, Singhal M, Xu L, Mendes P, Kummer U (2006) COPASI—a COMplex PATHway Simulator. *Bioinformatics* 22: 3067–3074
- Huang Z, Tajkhorshid E (2008) Dynamics of the extracellular gate and ion-substrate coupling in the glutamate transporter. *Biophys J* 95: 2292–2300
- Huysmans GH, Baldwin SA, Brockwell DJ, Radford SE (2010) The transition state for folding of an outer membrane protein. *Proc Natl Acad Sci USA* 107: 4099–4104
- Jiang J, Shrivastava IH, Watts SD, Bahar I, Amara SG (2011) Large collective motions regulate the functional properties of glutamate transporter trimers. *Proc Natl Acad Sci USA* 108: 15141–15146
- Johns GC, Somero GN (2004) Evolutionary convergence in adaptation of proteins to temperature: A4-lactate dehydrogenases of Pacific damselfishes (*Chromis* spp.). *Mol Biol Evol* 21: 314–320
- Juette MF, Terry DS, Wasserman MR, Altman RB, Zhou Z, Zhao H, Blanchard SC (2016) Single-molecule imaging of non-equilibrium molecular ensembles on the millisecond timescale. *Nat Methods* 13: 341–344
- Katoh K, Misawa K, Kuma K, Miyata T (2002) MAFFT: a novel method for rapid multiple sequence alignment based on fast Fourier transform. *Nucleic Acids Res* 30: 3059–3066
- Kortagere S, Fontana AC, Rose DR, Mortensen OV (2013) Identification of an allosteric modulator of the serotonin transporter with novel mechanism of action. *Neuropharmacology* 72: 282–290
- Kortagere S, Mortensen OV, Xia J, Lester W, Fang Y, Srikanth Y, Salvino JM, Fontana ACK (2018) Identification of novel allosteric modulators of glutamate transporter EAAT2. *ACS Chem Neurosci* 9: 522–534
- Kortzak D, Allea C, Weyand I, Ewers D, Zimmermann MI, Franzen A, Machtens JP, Fahlke C (2019) Allosteric gate modulation confers K(+) coupling in glutamate transporters. *EMBO J* 38: e101468
- Kramers HA (1940) Brownian motion in a field of force and the diffusion model of chemical reactions. *Physica* 7: 284–304
- Leffler JE (1953) Parameters for the description of transition states. *Science* 117: 340–341
- Leninger M, Sae Her A, Traaseth NJ (2019) Inducing conformational preference of the membrane protein transporter EmrE through conservative mutations. *Elife* 8: e48909
- Li Y, Hasenhuettl PS, Schicker K, Sitte HH, Freissmuth M, Sandtner W (2015) Dual action of Zn<sup>2+</sup> on the transport cycle of the dopamine transporter. *J Biol Chem* 290: 31069–31076
- Liao J, Marinelli F, Lee C, Huang Y, Faraldo-Gomez JD, Jiang Y (2016) Mechanism of extracellular ion exchange and binding-site occlusion in a sodium/calcium exchanger. *Nat Struct Mol Biol* 23: 590–599
- Low PS, Bada JL, Somero GN (1973) Temperature adaptation of enzymes: roles of the free energy, the enthalpy, and the entropy of activation. *Proc Natl Acad Sci USA* 70: 430–432
- Lu HP, Xun L, Xie XS (1998) Single-molecule enzymatic dynamics. *Science* 282: 1877–1882
- Matouschek A, Kellis Jr JT, Serrano L, Fersht AR (1989) Mapping the transition state and pathway of protein folding by protein engineering. *Nature* 340: 122–126

- McCoy AJ, Grosse-Kunstleve RW, Adams PD, Winn MD, Storoni LC, Read RJ (2007) Phaser crystallographic software. *J Appl Crystallogr* 40: 658–674
- Mihai C, Kravchuk AV, Tsai MD, Bruzik KS (2003) Application of Bronsted-type LFER in the study of the phospholipase C mechanism. *J Am Chem Soc* 125: 3236–3242
- Mim C, Tao Z, Grever C (2007) Two conformational changes are associated with glutamate translocation by the glutamate transporter EAAC1. *Biochemistry* 46: 9007–9018
- Min D, Jefferson RE, Qi Y, Wang JY, Arbing MA, Im W, Bowie JU (2018) Unfolding of a ClC chloride transporter retains memory of its evolutionary history. *Nat Chem Biol* 14: 489–496
- Moradi M, Enkavi G, Tajkhorshid E (2015) Atomic-level characterization of transport cycle thermodynamics in the glycerol-3-phosphate:phosphate antiporter. *Nat Commun* 6: 8393
- Mulligan C, Mindell JA (2013) Mechanism of transport modulation by an extracellular loop in an archaeal excitatory amino acid transporter (EAAT) homolog. *J Biol Chem* 288: 35266–35276
- Munro JB, Altman RB, O'Connor N, Blanchard SC (2007) Identification of two distinct hybrid state intermediates on the ribosome. *Mol Cell* 25: 505–517
- Nayak TK, Dana S, Raha S, Sikdar SK (2011) Activator-induced dynamic disorder and molecular memory in human two-pore domain hTREK1 K channel. *J Chem Biol* 4: 69–84
- Nguyen V, Wilson C, Hoemberger M, Stiller JB, Agafonov RV, Kutter S, English J, Theobald DL, Kern D (2017) Evolutionary drivers of thermoadaptation in enzyme catalysis. *Science* 355: 289–294
- Oh S, Boudker O (2018) Kinetic mechanism of coupled binding in sodium-aspartate symporter GltPh. *Elife* 7: e37291
- Otwinowski Z, Minor W (1997) Processing of X-ray diffraction data collected in oscillation mode. *Methods Enzymol* 276: 307–326
- Otzen DE, Itzhaki LS, elMasry NF, Jackson SE, Fersht AR (1994) Structure of the transition state for the folding/unfolding of the barley chymotrypsin inhibitor 2 and its implications for mechanisms of protein folding. *Proc Natl Acad Sci USA* 91: 10422–10425
- Paslawski W, Lillelund OK, Kristensen JV, Schafer NP, Baker RP, Urban S, Otzen DE (2015) Cooperative folding of a polytopic alpha-helical membrane protein involves a compact N-terminal nucleus and nonnative loops. *Proc Natl Acad Sci USA* 112: 7978–7983
- Rahman M, Ismat F, Jiao L, Baldwin JM, Sharples DJ, Baldwin SA, Patching SG (2017) Characterisation of the DAACS family *Escherichia coli* Glutamate/Aspartate-proton symporter GltP using computational, chemical, biochemical and biophysical methods. *J Membr Biol* 250: 145–162
- Rask-Andersen M, Masuram S, Fredriksson R, Schioth HB (2013) Solute carriers as drug targets: current use, clinical trials and prospective. *Mol Aspects Med* 34: 702–710
- Reimer LC, Vetcinina A, Carbasse JS, Sohngen C, Gleim D, Ebeling C, Overmann J (2019) BacDive in 2019: bacterial phenotypic data for High-throughput biodiversity analysis. *Nucleic Acids Res* 47: D631–D636
- Renosto F, Schultz T, Re E, Mazer J, Chandler CJ, Barron A, Segel IH (1985) Comparative stability and catalytic and chemical properties of the sulfate-activating enzymes from *Penicillium chrysogenum* (mesophile) and *Penicillium duponti* (thermophile). *J Bacteriol* 164: 674–683
- Reyes N, Ginter C, Boudker O (2009) Transport mechanism of a bacterial homologue of glutamate transporters. *Nature* 462: 880–885
- Reyes N, Oh S, Boudker O (2013) Binding thermodynamics of a glutamate transporter homolog. *Nat Struct Mol Biol* 20: 634–640
- Rice P, Longden I, Bleasby A (2000) EMBOSS: the European molecular biology open software suite. *Trends Genet* 16: 276–277
- Rives ML, Javitch JA, Wickenden AD (2017) Potentiating SLC transporter activity: emerging drug discovery opportunities. *Biochem Pharmacol* 135: 1–11
- Ruan Y, Miyagi A, Wang X, Chami M, Boudker O, Scheuring S (2017) Direct visualization of glutamate transporter elevator mechanism by high-speed AFM. *Proc Natl Acad Sci USA* 114: 1584–1588
- Ryan RM, Compton EL, Mindell JA (2009) Functional characterization of a Na<sup>+</sup>-dependent aspartate transporter from *Pyrococcus horikoshii*. *J Biol Chem* 284: 17540–17548
- Ryan RM, Kortt NC, Sirivanta T, Vandenberg RJ (2010) The position of an arginine residue influences substrate affinity and K<sup>+</sup> coupling in the human glutamate transporter, EAAT1. *J Neurochem* 114: 565–575
- Saavedra HG, Wrabl JO, Anderson JA, Li J, Hilser VJ (2018) Dynamic allostery can drive cold adaptation in enzymes. *Nature* 558: 324–328
- Schlebach JP, Woodall NB, Bowie JU, Park C (2014) Bacteriorhodopsin folds through a poorly organized transition state. *J Am Chem Soc* 136: 16574–16581
- Selvam B, Mittal S, Shukla D (2018) Free energy landscape of the complete transport cycle in a key bacterial transporter. *ACS Cent Sci* 4: 1146–1154
- Shrivastava IH, Jiang J, Amara SG, Bahar I (2008) Time-resolved mechanism of extracellular gate opening and substrate binding in a glutamate transporter. *J Biol Chem* 283: 28680–28690
- Sigworth FJ, Sine SM (1987) Data transformations for improved display and fitting of single-channel dwell time histograms. *Biophys J* 52: 1047–1054
- Somero GN (2004) Adaptation of enzymes to temperature: searching for basic "strategies". *Comp Biochem Physiol B Biochem Mol Biol* 139: 321–333
- Sorum B, Czege D, Csanady L (2015) Timing of CFTR pore opening and structure of its transition state. *Cell* 163: 724–733
- Stelzl LS, Fowler PW, Sansom MS, Beckstein O (2014) Flexible gates generate occluded intermediates in the transport cycle of LacY. *J Mol Biol* 426: 735–751
- Stolzenberg S, Khelashvili G, Weinstein H (2012) Structural intermediates in a model of the substrate translocation path of the bacterial glutamate transporter homologue GltPh. *J Phys Chem B* 116: 5372–5383
- Thomas TM, Scopes RK (1998) The effects of temperature on the kinetics and stability of mesophilic and thermophilic 3-phosphoglycerate kinases. *Biochem J* 330(Pt 3): 1087–1095
- Tolner B, Ubbink-Kok T, Poolman B, Konings WN (1995) Characterization of the proton/glutamate symport protein of *Bacillus subtilis* and its functional expression in *Escherichia coli*. *J Bacteriol* 177: 2863–2869
- Vandenberg RJ, Ryan RM (2013) Mechanisms of glutamate transport. *Physiol Rev* 93: 1621–1657
- Verdon G, Boudker O (2012) Crystal structure of an asymmetric trimer of a bacterial glutamate transporter homolog. *Nat Struct Mol Biol* 19: 355–357
- Verdon G, Oh S, Serio RN, Boudker O (2014) Coupled ion binding and structural transitions along the transport cycle of glutamate transporters. *Elife* 3: e02283
- Wang J, Albers T, Grever C (2018) Energy landscape of the substrate translocation equilibrium of plasma-membrane glutamate transporters. *J Phys Chem B* 122: 28–39
- Wang X, Boudker O (2020) Large domain movements through the lipid bilayer mediate substrate release and inhibition of glutamate transporters. *Elife* 9: e58417
- Weng J, Fan K, Wang W (2012) The conformational transition pathways of ATP-binding cassette transporter BtuCD revealed by targeted molecular dynamics simulation. *PLoS One* 7: e30465

- Weng JW, Fan KN, Wang WN (2010) The conformational transition pathway of ATP binding cassette transporter MsbA revealed by atomistic simulations. *J Biol Chem* 285: 3053–3063
- Wu C, Wynne SA, Thomas NE, Uhlemann EM, Tate CG, Henzler-Wildman KA (2019) Identification of an alternating-access dynamics mutant of EmrE with impaired transport. *J Mol Biol* 431: 2777–2789
- Xue Q, Yeung ES (1995) Differences in the chemical reactivity of individual molecules of an enzyme. *Nature* 373: 681–683
- Yernool D, Boudker O, Folta-Stogniew E, Gouaux E (2003) Trimeric subunit stoichiometry of the glutamate transporters from *Bacillus caldotenax* and *Bacillus stearothermophilus*. *Biochemistry* 42: 12981–12988
- Yernool D, Boudker O, Jin Y, Gouaux E (2004) Structure of a glutamate transporter homologue from *Pyrococcus horikoshii*. *Nature* 431: 811–818
- Zheng Q, Jockusch S, Zhou Z, Blanchard SC (2014) The contribution of reactive oxygen species to the photobleaching of organic fluorophores. *Photochem Photobiol* 90: 448–454
- Zhuang X, Kim H, Pereira MJ, Babcock HP, Walter NG, Chu S (2002) Correlating structural dynamics and function in single ribozyme molecules. *Science* 296: 1473–1476
- Zomot E, Bahar I (2013) Intracellular gating in an inward-facing state of aspartate transporter Glt(Ph) is regulated by the movements of the helical hairpin HP2. *J Biol Chem* 288: 8231–8237
- Zorba A, Nguyen V, Koide A, Hoemberger M, Zheng Y, Kutter S, Kim C, Koide S, Kern D (2019) Allosteric modulation of a human protein kinase with monobodies. *Proc Natl Acad Sci USA* 116: 13937–13942
- Zosel F, Mercadante D, Nettels D, Schuler B (2018) A proline switch explains kinetic heterogeneity in a coupled folding and binding reaction. *Nat Commun* 9: 3332
- Zwanzig R (1990) Rate processes with dynamical disorder. *Acc Chem Res* 23: 148–152



**License:** This is an open access article under the terms of the Creative Commons Attribution-NonCommercial-NoDerivs 4.0 License, which permits use and distribution in any medium, provided the original work is properly cited, the use is non-commercial and no modifications or adaptations are made.